



Atmospheric photochemistry

Franck Lefèvre, Vladimir Krasnopolsky

► To cite this version:

Franck Lefèvre, Vladimir Krasnopolsky. Atmospheric photochemistry. Robert M. Haberle R. Todd Clancy François Forget Michael D. Smith Richard W. Zurek (eds). The Atmosphere and Climate of Mars, chapitre 13, Cambridge University Press, pp.405-432, 2017, 978-1-107-01618-7. 10.1017/9781139060172.013 . insu-01629833

HAL Id: insu-01629833

<https://insu.hal.science/insu-01629833>

Submitted on 2 Aug 2021

HAL is a multi-disciplinary open access archive for the deposit and dissemination of scientific research documents, whether they are published or not. The documents may come from teaching and research institutions in France or abroad, or from public or private research centers.

L'archive ouverte pluridisciplinaire **HAL**, est destinée au dépôt et à la diffusion de documents scientifiques de niveau recherche, publiés ou non, émanant des établissements d'enseignement et de recherche français ou étrangers, des laboratoires publics ou privés.

Chapter 13: Atmospheric Photochemistry

Revised version

9 october 2015

Franck Lefèvre

LATMOS, CNRS, Université Pierre et Marie Curie,

Boîte 102, F-75005 Paris, France.

Vladimir Krasnopolsky

Department of Physics, Catholic University of America,

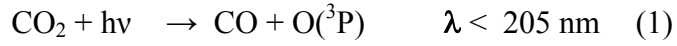
Washington, DC 20064, USA.

13.1 INTRODUCTION

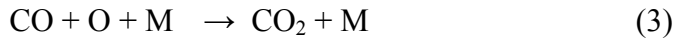
The bulk atmosphere of Mars is almost entirely composed of CO₂ with small amounts of N₂ and Ar and trace amounts of H₂O (Table 13.1). As a result, the only processes that can initiate martian photochemistry are the photolysis of CO₂ and H₂O by ultraviolet solar light. Therefore, martian photochemistry can be summarized by the interactions between oxygenated products of CO₂ and hydrogen products of H₂O. This picture is much simpler than that of other planetary atmospheres of our solar system. For instance, contrary to Earth or Titan, nitrogen chemistry plays a minor role on Mars. And unlike Earth and Venus, chlorine and sulfur chemistries have not been identified. Also, Mars lacks the richness of the organic chemistry observed in Earth's troposphere, the giant planets, and Titan. Yet, despite this apparent simplicity, it must be recognized that martian photochemistry is still not completely understood. As we will show in this chapter, significant progress has been made in our understanding of the short-lived species that determine the equilibrium state of the martian atmosphere, such as ozone (O₃) or hydrogen peroxide (H₂O₂). However, for longer-lived species the situation is less satisfactory. In particular, the abundance of CO – the product of CO₂ photolysis – has been and remains an unsolved challenge for chemical models. The fact that such a basic problem persists after decades of research may be indicative that an important process is missing or largely inaccurate in our understanding of the Mars photochemical system.

It was revealed in the 1960s (e.g., Kliore *et al.*, 1965; Belton and Hunten, 1966; Kaplan *et al.*, 1969) that Mars could maintain an almost pure atmosphere of CO₂ (95.5%) with only trace amounts of its photodissociation products CO (volume mixing ratio of $\sim 9 \times 10^{-4}$), O ($\sim 10^{-3}$ at 100 km), and O₂ (1.4×10^{-3}) (Table 13.1). At the time of that discovery, the remarkable stability of

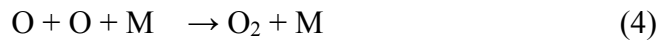
Mars CO₂ was in striking contradiction with the known kinetics of a pure CO₂ atmosphere exposed to sunlight. Indeed, solar ultraviolet radiation penetrates all the way to the surface in the thin martian atmosphere and photodissociates CO₂ into carbon monoxide and atomic oxygen in its ground state O(³P) or its excited state O(¹D):



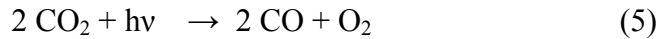
For clarity O(³P) will be denoted as O in the following of this chapter. Once CO₂ is photodissociated it is difficult to restore it since the reverse reaction,



is spin-forbidden and therefore very slow (M represents a third body, usually CO₂ on Mars). Thus, the photolysis of CO₂ should in principle lead to a large buildup of CO and O. In addition, copious amounts of O₂ should be formed by the collision of oxygen atoms, which is about a hundred times more efficient than reaction (3):



The net result of CO₂ photolysis is therefore



This suggests a production of CO and O₂ at a ratio of 2:1, only compensated by the slow reaction (3) and by the photolysis of O₂, which prevents O₂ to build up indefinitely:



A theoretical model of the photochemistry of a pure CO₂ atmosphere can be constructed from the set of reactions (1-6). The results of such a model are however in disagreement with the observations. The obtained mixing ratios of CO and O₂ are two orders of magnitude larger than the measured quantities (0.08 and 0.04 respectively, as calculated for instance by Nair et al., 1994), and their 2:1 ratio is also opposite to the ~1:2 observed CO:O₂ ratio. These large differences were puzzling until the classic papers of McElroy and Donahue (1972) and Parkinson and Hunten (1972) showed that the composition of the Mars atmosphere could be precisely controlled by the “odd hydrogen” species (H, OH, HO₂, known as HO_x) produced by the photolysis of water vapor. Although HO_x are only present in trace amounts of a few parts per billion (ppbv), we will show in section 13.2 that these short-lived species can catalytically convert CO into CO₂ at a rate that is orders of magnitude faster than the direct reaction (3). In fact, this process is so efficient that photochemical models now have the opposite problem of underestimating CO relative to the observations. In section 13.3 we will present the chemistry of oxygen and some of the large advances accomplished during the last decade in the observational knowledge of these compounds. The role of nitrogen species, which is poorly constrained by observations, will be described in section 13.4. We will examine the possibility of sulfur and chlorine chemistry in section 13.5. In section 13.6, we will discuss the discovery of low levels of methane claimed by several teams since 2004, and also detected over a short period at the surface of Mars by the Curiosity rover. Finally, we will conclude (section 13.7) by a summary of

the current strengths and weaknesses of photochemical models and the outstanding issues in our quantitative understanding of martian photochemistry.

We will only address in this chapter the photochemistry of the low and middle atmosphere up to about 100 km. The active chemistry taking place in the thermosphere is specifically addressed in Chapter 14 (Upper Atmosphere and Ionosphere).

13.2 HYDROGEN CHEMISTRY

In the lower atmosphere of Mars, the primary sources of odd hydrogen (HO_x) are the photolysis of water vapor:




and its oxidation by atomic oxygen in its excited state $\text{O}(^1\text{D})$:



The latter process plays an important role in the lowest scale height near the surface. Above that level and up to the condensation level of water vapor (known as the hygropause), the photolysis of H_2O in (7) largely dominates the production of HO_x . This photolysis occurs in the same spectral domain as CO_2 and is therefore highly dependent on the overhead column of CO_2 (and near the surface, to dust loading). For example, at a solar zenith angle of 60° , a mean sun distance of 1.52 AU and a visible dust opacity of 0.6, the H_2O photolysis frequency increases

from $4 \times 10^{-11} \text{ s}^{-1}$ near the martian surface (at 6 hPa) to $2 \times 10^{-8} \text{ s}^{-1}$ at 40 km. Even at this latter level, the timescale of the H_2O photolysis remains longer than one terrestrial year. Yet, this slow photolysis is sufficient to produce the few parts per billion (ppbv) of HO_x that contribute, as we will show in the following, to the chemical stability of the Mars atmosphere.

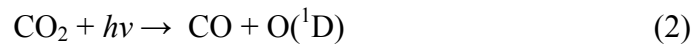
The seasonal evolution of water vapor on Mars is now well documented by a large dataset of satellite observations. At high latitudes, sublimation and condensation processes near the pole lead to the alternation of a strong spring/summer seasonal maximum (30-50  μm) and a very dry (< 1 precipitable- μm) vortex in winter (Figure 13.1). Atmospheric transport propagates a fraction of this signal towards mid-to-low latitudes where H_2O seasonal variations are lesser around a mean value of ~ 10 precipitable- μm (see Chapter 11, The Water Cycle, for more details). This general pattern is only representative of the vertically-integrated H_2O column. Because of the strong altitude dependence of the H_2O photolysis in (7), it is very important to consider how H_2O is distributed along the vertical to understand the seasonal variations of the production rate of HO_x . The vertical distribution of H_2O is known to vary by a large extent with latitude, season, local time, and the local meteorological situation. For instance, ground-based (Clancy et al., 1996) and satellite (Maltagliati et al., 2011; 2013) measurements have shown that orbital changes in temperature at low and middle latitudes lead to a dramatic rise of the hygropause from 10 km around aphelion ($L_s = 71^\circ$) up to 50 km around perihelion ($L_s = 251^\circ$). This behavior of H_2O is well reproduced by three-dimensional models (see Figure 13.2 and Montmessin et al., 2004). Even above the hygropause, models indicate that the warm, dusty atmosphere of perihelion can carry about a thousand times more H_2O than during the dust-free, cold aphelion period. The difference in the altitude of water vapor saturation -or sometimes supersaturation (Maltagliati et al., 2011)- and the amount of H_2O

allowed to cross that cold trap have a dramatic impact on the amount of HO_x produced in the middle and upper atmosphere. This is illustrated in Figure 13.2 where global climate model simulations predict a two order of magnitude increase of odd hydrogen species HO_x from aphelion to perihelion.

In fact, the dryness of the middle and upper atmosphere at aphelion is such that the role of H₂O as a source of HO_x may be severely reduced. In these conditions, an important source of HO_x becomes then the oxidation of H₂ by O(¹D):



This process is less efficient than H₂O photolysis. However, in the dry conditions of aphelion, reaction (9) is the dominant HO_x production term at all altitudes above ~30 km. O(¹D) is produced by photolysis of ozone in the lower and middle atmosphere, which is weakly dependent on the solar zenith angle. Therefore, reaction (9) also plays also a major role in the production of HO_x in the dehydrated regions at the sunlit edge of the polar night in winter. In the upper atmosphere, O(¹D) is one product of CO₂ photolysis by ultraviolet radiation (reaction (2)), which becomes more and more available as altitude increases and the CO₂ opacity decreases. Thus, similar to H₂O photolysis in (7), the efficiency of reaction (9) at producing hydrogen radicals increases with altitude. It results from both processes that the total HO_x mixing ratio is a maximum in the upper atmosphere, with amounts varying from ~100 to ~10000 ppbv at 100 km, depending on the amount of H₂O at this level (Figure 13.3). At high altitude, HO_x is entirely in the form of H. The OH formed in (7-9) is indeed rapidly converted in (11) to H by the abundant O atoms that result from CO₂ photolysis and the quenching of O(¹D):



In the lower atmosphere, less O is available for reaction (11) and the main loss process of OH is in this case the reaction with CO, which forms CO₂:



The hydrogen atom H obtained in (12) reacts in turn with O₂:



The rate of this three-body reaction strongly increases with pressure. This explains why H has a very short lifetime (~1s) in the lower atmosphere and is rapidly removed by reaction (13) to make the hydroperoxy radical HO₂ the dominant form of HO_x near the surface (Figure 13.3). Between both regimes (H-dominated at high altitudes, HO₂-dominated at low altitudes), OH is usually the main HO_x species in the middle atmosphere.

The production of HO₂ in (13) is at photochemical equilibrium with the fast loss reaction with the O atoms produced by CO₂ photolysis:



which recycles the OH initially lost in reaction (12).

This sequence of reactions (12-14) can therefore be represented by the following cycle, first proposed by McElroy and Donahue (1972):

Cycle I



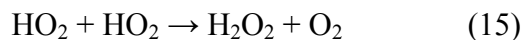
The net result of cycle I is the reformation of CO_2 from its photolysis product CO. According to model simulations (Nair et al., 1994; Yung and DeMore, 1999; Krasnopolsky, 2010), it contributes to about 85% of the recycling of CO into CO_2 in the Mars atmosphere. It is important to note that odd hydrogen is not lost in these cycles and therefore acts as a catalyst. From Table 13.2 it can be seen that the column-integrated loss rate of CO determined by (12) is about 100 times larger than the production rate of HO_x determined by H_2O photolysis. Thus, every HO_x radical produced by H_2O is used about 100 times in cycle I (and its variants presented in the following) to reform CO_2 before it is returned to a less reactive form of hydrogen. The reaction (12) is the major process of formation of the CO-O bond that balances the breaking of this bond by the photolysis of CO_2 . However, the production and loss rates of CO are not in local equilibrium. In the middle and upper atmosphere, the lack of OH makes reaction (12) inefficient

and CO is produced without any significant loss (Figure 13.4). In contrast, between the surface and the hygropause, the CO loss rate by reaction (12) exceeds its production. CO has therefore a slow negative trend in the lower atmosphere, where its lifetime is of ~ 5 terrestrial years. This long lifetime does not authorize chemical variations of CO with local time or even at the seasonal timescale. Yet, observations show a pronounced seasonal cycle of the CO mixing ratio at high latitudes (Figure 13.5), with an enhancement of more than a factor of two in winter and a depletion of the same order of magnitude in summer (Krasnopolsky, 2003a; Encrenaz et al., 2006; Krasnopolsky, 2007; Smith et al., 2009). This phenomenon is not of chemical origin. It is a response to the condensation/sublimation cycle of CO₂ to and from the seasonal ice caps, which leads to enrichment/depletion of all non-condensable gases in polar regions, as also seen in observations of argon (Sprague et al., 2004).

The global photochemical equilibrium of the martian atmosphere therefore results from a subtle balance between the CO production (CO₂ loss), occurring throughout the atmosphere during the day, and the CO loss (CO₂ production) that occurs between the surface and the hygropause. Vertical mixing maintains a roughly constant CO mixing ratio in the lower atmosphere up to ~ 50 km. Measurements of martian CO carried out from space or from the Earth converge towards a mean value of 900-1100 ppmv at middle latitudes (Krasnopolsky, 2007; Billebaud et al., 2009; Hartogh et al., 2010a; Sindoni et al., 2011). The most complete CO dataset, obtained with the CRISM instrument on board Mars Reconnaissance Orbiter (Smith et al., 2009), indicates a lower globally-averaged value of ~ 700 ppmv, with strong seasonal variations at high latitudes (Figure 13.5).

The amount of OH available for reaction (12) obviously plays a critical role in the equilibrium value of CO. As OH is a product of H₂O photolysis, it is essential to represent properly the strong variations of H₂O over the martian year in models aimed at a quantitative understanding of martian photochemistry. Clancy and Nair (1996) illustrated this problem by using a one-dimensional (1D) model forced by a stepwise annual cycle of the water vapor profile. They showed that the variations of the condensation level of H₂O between perihelion and aphelion is the source of up to a two orders of magnitude variation in HO_x density at 20-40 km, implying that the rate of the CO₂ recycling also varies considerably over one annual cycle.

Another indirect product of H₂O photolysis is the hydrogen peroxide H₂O₂ formed by the self-reaction of radicals HO₂:

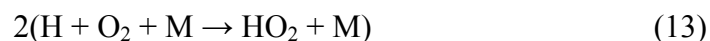
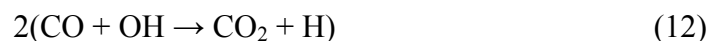


Hydrogen peroxide is recognized to be a powerful oxidizer of organic material as confirmed by laboratory experiments (Quinn and Zent, 1999; Gough et al., 2011). Mineral processing of H₂O₂ in the martian surface could also lead to highly reactive hydrogen radicals or superoxides (Atreya et al., 2011) and might explain the apparent absence of organics as revealed by the Viking experiments (Biemann et al., 1976). It is evident from reaction (15) that the production of H₂O₂ is quadratically dependant on the concentration of HO₂ (and hence, of H₂O). Models therefore predict H₂O₂ to be essentially confined to the first 20-30 km above the surface where HO₂ is most abundant (Figure 13.6). During the day, the formation of H₂O₂ is close to photochemical equilibrium with its loss by photolysis:



which occurs with a typical timescale of ~6 hours. This is significantly slower than the loss processes of H, OH, HO₂ that occur in a few seconds to minutes in the lower atmosphere. H₂O₂ can therefore accumulate from HO₂, and act as a temporary reservoir of HO_x. H₂O₂ also contributes to the reformation of CO₂ and to the stability of the Mars atmosphere through the following variant of cycle I, obtained when the HO₂ produced in (13) reacts with itself to form H₂O₂ rather than with O:

Cycle II



Photochemical models estimate that this cycle initially proposed by Parkinson and Hunten (1972) contributes to about 8% of the total restoration of CO₂ from CO (Nair et al., 1994; Yung and DeMore, 1999; Krasnopolsky, 2010).

The fact that H₂O₂ is a measurable species that provides quasi-direct quantitative information on the amount of HO_x makes it a desirable target for observers. After years of searching, H₂O₂ was finally detected in 2003 by two independent measurements performed from Earth (Clancy et al.,

2004; Encrenaz et al., 2004). These data as well as those obtained in the following years (Encrenaz et al., 2008, 2012; Hartogh et al., 2010a) indicate a substantial seasonal evolution of the H_2O_2 mixing ratio from less than 10 ppbv around aphelion to more than 30 ppbv at $L_s = 210^\circ$ (Figure 13.7). The pronounced H_2O_2 minimum observed at aphelion occurs, surprisingly, when its primal source H_2O is largest. This phenomenon contradicts the expected H_2O - HO_x correlation and cannot be explained by models only considering the known gas-phase chemistry. However, it can be somewhat improved by models including heterogeneous chemical reactions on the water-ice clouds that form in this season (Krasnopolsky, 2006a, 2009; Lefèvre et al., 2008). The H_2O_2 dataset thus may provide a clue that heterogeneous processes (discussed in section 13.7) play a role in lowering the amount of HO_x and the oxidation rate of CO at certain times of the year, even though the very low upper limits for H_2O_2 determined by Encrenaz et al. (2002) and Hartogh et al. (2010a) are still challenging to reproduce and will require further investigation.

The cycles that oxidize CO into CO_2 terminate when the catalyzer HO_x is irreversibly returned to a long-lived form of hydrogen. The most efficient reaction of this type is:



which reforms the stable species H_2O and limits the amount of HO_x that can exist in the atmosphere. Reaction (17) is therefore of fundamental importance for a quantitative understanding of martian atmospheric chemistry. Unfortunately, this has been a difficult reaction to study. The recommended reaction rate is still subject to a large uncertainty at martian temperatures (Sander et al., 2011). A minor contribution to the removal of HO_x also exists via the reaction between H and HO_2 , forming either molecular hydrogen or water vapor:



Most of the production of H_2 in (18) is balanced by its loss reactions with OH (80% of the loss) and $\text{O}(^1\text{D})$ (20%):



The chemistry of H_2 is very slow in the lower atmosphere, where its lifetime is of the order of 300 terrestrial years. H_2 can therefore be transported passively to high altitudes where the molecule is essentially destroyed by ionospheric reactions. These processes produce H atoms which may then escape to space. H_2 was detected in the upper atmosphere of Mars by Krasnopolsky and Feldman (2001) using the Far Ultraviolet Spectroscopic Explorer. Extrapolation of the observed abundances to the middle and lower atmosphere resulted in a mixing ratio of 17 ppmv (Table 13.1). Finally, odd hydrogen may also be removed by condensation of H_2O_2 and precipitation of solid H_2O_2 onto the surface. This process is calculated to occur at $T < 180 \text{ K}$ for a H_2O_2 mixing ratio of $\sim 10 \text{ ppbv}$ and a pressure of 6 hPa (Kong and McElroy, 1977b ; Lindner, 1988).

13.3 OXYGEN CHEMISTRY

On Earth, the reactive forms of oxygen O, $\text{O}(^1\text{D})$, and O_3 result from the photolysis of O_2 which is itself produced in large amounts (21% of the total composition) by photosynthesis. In

the absence of such process on Mars, O₂ has to be formed photochemically and is present in much smaller quantities. The first Earth-based measurements of martian O₂ used the lines of the O₂ band at 762 nm and indicated a mixing ratio of 1.2x10⁻³ (Barker, 1972; Carleton and Traub, 1972; Trauger and Lunine, 1983). Observations performed in the submillimeter range from the Herschel/HIFI instrument have derived a mean O₂ mixing ratio of 1.4x10⁻³ (Hartogh et al., 2010a). The only in-situ measurement of O₂ was performed by the Sample Analysis at Mars (SAM) suite of instruments on board on the Curiosity rover (Mahaffy et al., 2013). The O₂ mixing ratio reported from SAM is 1.45x10⁻³, in very good agreement with the previous Herschel observations.

As mentioned in section 13.1, the most evident pathway to form O₂ in a CO₂ atmosphere is the recombination of O atoms via:



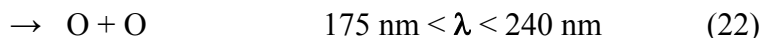
On Mars, this reaction plays an important role in the production of O₂ above 50 km but represents only ~10% of the formation rate of the O-O bond integrated over the whole atmosphere. Due to the presence of OH in the middle and lower atmosphere, a much more efficient process to form the O-O bond is the reaction:



which is responsible for ~90% of the O₂ production on Mars. O₂ can therefore be considered as an indirect product of the CO₂ and H₂O photolysis, since these processes provide the reactants O

and OH of reaction (11). This gives another illustration of the importance of the HO_x radicals in regulating martian atmospheric chemistry. Reactions (14, 15, 17, 18) producing O₂ from the reactant HO₂ are not considered as production mechanisms of O₂ since one O₂ molecule is used in (13) to form HO₂.

The main (75%) loss process of O₂ occurs through reaction (13) with H, but this reaction does not break the O-O bond and O₂ is immediately returned by reaction (14) between HO₂ and O. The primary process breaking the O-O bond is the O₂ photolysis:



Although the O₂ photolysis represents a minor channel (<5%) in terms of instantaneous loss of O₂, this mechanism accounts for ~50% of the total destruction of the O-O bond in the Mars atmosphere. Other important processes to consider are the photolysis of HO₂ and H₂O₂, as well as the reaction:



These three processes all produce OH and account for ~30% of the breaking of the O-O bond. The remaining ~20% is theoretically accomplished by the reaction between NO and HO₂, if one assumes a mean amount of 0.6 ppbv of nitrogen oxides in the low atmosphere (see section 13.4). From these various loss processes, the mean lifetime of O₂ in the Mars atmosphere is estimated to be ~60 years (Krasnopolsky, 2010). O₂ is therefore expected to be uniformly mixed by

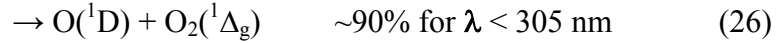
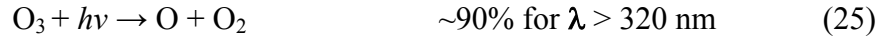
atmospheric transport, and should be only subject to slow seasonal variations induced by the condensation and sublimation cycle of CO₂ in polar regions.

Due to the low abundance of O₂, the O₂ photolysis in (21-22) is not like on Earth the main contributor to the production of what is generally referred as the “odd oxygen” family, or O_x = O(¹D) + O + O₃. On Mars this role is played at ~80% by the CO₂ photolysis, which produces rapidly increasing amounts of O atoms with altitude. At 100 km, the O mixing ratio may reach values of several thousands of ppmv that approach those of CO (Figure 13.8), the other direct product of CO₂ photolysis.

The loss process of O atoms depends on the altitude. In the thermosphere and down to ~70 km, the only significant sink of O is reaction (4). This reaction is slow and authorizes a chemical lifetime of several months for the O_x family that is dominated by O in the upper atmosphere (Figure 13.9). O atoms may therefore be transported quasi-passively by the Hadley circulation from their region of production into the polar night, where they are brought towards lower altitudes by the downwelling motion above the winter pole (Figure 13.8). In the middle and lower atmosphere, the main sink of O atoms is the well-known three-body reaction with O₂ leading to the formation of ozone:



This reaction is a loss of O but is null in terms of O_x since O₃ is produced. In the sunlit portion of the atmosphere, the inverse process returning O from O₃ within the O_x family is the O₃ photolysis, which occurs at a timescale shorter than 5 minutes at all altitudes:



where the $\text{O}({}^1\text{D})$ produced in (26) is then rapidly quenched by CO_2 in reaction (10). Thus, the reactions of exchange between O , $\text{O}({}^1\text{D})$, and O_3 are fast and each of those species is at photochemical equilibrium during the day within the O_x family. For ozone, the daytime steady-state expression for production and loss leads to the following ratio of abundances:

$$\frac{O_3}{O} = \frac{k_{24} [O_2][CO_2]}{J_{O_3}} \quad (27)$$

where k_{24} is the reaction rate ($\text{cm}^6 \text{ s}^{-1}$) of reaction (24) and J_{O_3} is photolysis frequency (s^{-1}) of ozone. This ratio is of the order of ~ 1 at 25 km and of ~ 50 -100 near the surface. O_3 is therefore the dominant O_x species in the lower atmosphere. It is also the only O_x species that is directly measurable by remote sensing, thanks to its strong absorption bands both in the ultraviolet (255 nm) and in the infrared (9.6 μm). These properties allow relatively easy access to the abundance of O_3 in the martian atmosphere, provided that the observation is performed outside the ozone-rich Earth atmosphere, or that the terrestrial absorption can be eliminated by Doppler shift. Early in the space age, martian O_3 was searched for and discovered by the Mariner ultraviolet spectrometers in 1969 and 1971-72 (Barth and Hord, 1971; Barth et al., 1973). The first positive measurements were of O_3 columns of 10-50 $\mu\text{m-atm}$ and were only found in the polar regions. This must be compared to the Earth globally-averaged O_3 column of $\sim 3 \text{ mm-atm}$. With such low quantities, ozone on Mars does not offer an efficient shield comparable to the Earth ozone layer

against solar ultraviolet radiation and all wavelengths larger than 200 nm can reach the martian surface. The ultraviolet spectrometer of Mariner also revealed that ozone is strongly variable on Mars. While positive detections were obtained at high latitudes in winter-spring, ozone was below the detection limit of the instrument ($3 \mu\text{m-atm}$) equatorward of 45° latitude during any season. Lane et al. (1973) noted a rise in ozone measured by Mariner 9 when water vapor froze out of the atmosphere. This fact was reproduced by the modeling studies that followed in the late 1970s (e.g., Liu and Donahue 1976; Kong and McElroy, 1977b; Krasnopolsky and Parshev, 1979; Shimazaki and Shimizu, 1979), which highlighted the crucial role played by H_2O and its photolysis products HO_x in the chemistry and variations of ozone. This role is easy to understand since model calculations show that the strongest sink of O_x in the lower and middle atmosphere is:



This reaction suppresses irreversibly the O atoms otherwise used in (24) to form O_3 . It is also one of key steps of the Cycle I described in section 13.2. The efficiency of this catalytic cycle is such, that the chemical lifetime of O_x determined by reaction (14) is, during the day, shorter than 1 hour at low-to-middle latitudes below 25 km (Figure 13.9). Ozone, the main form of O_x at those altitudes, is therefore quite sensitive to the amount of HO_2 and is expected to be anti-correlated to H_2O , the source of HO_x . This tight coupling makes O_3 a useful tracer of the odd hydrogen chemistry that stabilizes the CO_2 atmosphere of Mars, and O_3 measurements offer a powerful constraint for photochemical models.

There has been much progress in recent years in the knowledge of the climatology of O_3 on Mars, which is the short-lived species best described by the observation. Latitudinal cross-sections of the O_3 column at several Mars seasons have been obtained from the Earth using infrared heterodyne spectroscopy (Espenak et al., 1991; Fast et al., 2006, 2009) and from the Hubble Space telescope in the ultraviolet range (Clancy et al., 1999). Since 2004, the SPICAM ultraviolet spectrometer on board Mars Express has also been providing a near-complete coverage of the O_3 column distribution (Perrier et al., 2006), as well as the first observations of the O_3 nighttime distribution (Lebonnois et al., 2006). All these measurements have clearly identified the anti-correlation between O_3 and H_2O that is predicted by the photochemical theory. A significant example is provided by the O_3 column climatology obtained by SPICAM in three martian years of observation (Figure 13.10), which is most of the time inversely related to the H_2O column abundance as measured by TES (Figure 13.1). Compared to Earth, the very strong seasonal and spatial variability of ozone (a factor of ~ 100 as opposed to ~ 3 on our planet) is a striking feature of martian photochemistry. As for Mariner the maximum abundances of ozone measured by SPICAM are near $40 \mu\text{m-atm}$ and are found at high latitudes in winter, when the absence of water vapor and lack of sunlight prevent almost completely the production of HO_x . In these conditions, the chemical lifetime of ozone may increase from its typical value of ~ 1 hour up to several days, and ozone can accumulate inside the polar vortex. This is especially true at polar low altitudes (Figure 13.8), where model simulations predict that ozone is not reached by the ozone-destroying HO_x produced by the descent of H atoms from the thermosphere (Figure 13.3). This model calculation is also supported by the observations of the vertical distribution of O_3 performed by SPICAM in stellar occultation mode, showing that most of the polar ozone (in terms of number density) is confined below 20 km in winter (Lebonnois et al., 2006). Recently, a further analysis of SPICAM polar night data also revealed the presence of a secondary O_3 layer

between 30-60 km that is only present in the southern hemisphere (Montmessin and Lefèvre, 2013; Figure 13.11). This layer is well reproduced by GCM simulations (Figure 13.8) and shows O₃ mixing ratios larger than anywhere else (0.5-1.5 ppmv) on the planet at this time of the year. Its formation is related to the deep vertical downwelling of O-rich air masses by the Hadley circulation, visible in Figure 13.8, which promotes the formation of ozone by reaction (24). The fact that no elevated O₃ polar layer is observed in the northern hemisphere can be explained by the much larger H amounts that are present near the north pole at that time of year (see Figure 13.3). As the reaction



is the main ozone-loss process above 20 km in the polar night, the destruction of ozone is about 100 times stronger above the northern winter pole than above its southern counterpart, which prevents a significant buildup of polar ozone in the middle atmosphere. The OH radicals produced in (28) are vibrationally excited and are a source of near infrared emission (Mainel band) in the upper terrestrial mesosphere (Bates and Nicolet, 1950). Recently this OH emission was detected for the first time on Mars from CRISM limb observations of polar night (Clancy et al., 2013a). The emission was observed in a distinct layer between 40-55 km. GCM simulations show that the OH polar nightglow is stimulated by the descent of H atoms from the thermosphere, which provides a further indication of the deep Hadley solstitial circulation of the Mars atmosphere.

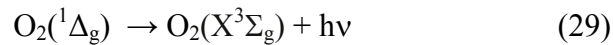
In terms of integrated ozone vertical column, in the polar vortices only the large concentrations of ozone located near the surface are significant. In these conditions the photochemistry is slow

and atmospheric transport plays a major role. Three-dimensional model simulations have shown (Lefèvre et al., 2004) that the confinement of large O₃ column amounts inside the polar vortex and the dynamical disturbances in the shape of the vortex caused by wave activity can explain the considerable day-to-day variability in ozone measured at high latitudes by Mariner (Traub et al., 1979), SPICAM (Perrier et al., 2006), and the MARCI imager on Mars Reconnaissance Orbiter (Clancy et al., 2014).

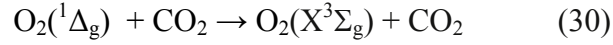
The ozone annual cycle at low latitudes is of much more limited amplitude than at high latitudes. Ultraviolet measurements performed with the HST (Clancy et al., 1999), later confirmed by infrared observations from the Earth (Fast et al., 2006), gave evidence of a broad maximum of 2-6 $\mu\text{m-atm}$ centered on Mars aphelion, which contrasts with O₃ columns of $\sim 1 \mu\text{m-atm}$ shortly after equinox (Figure 13.12). At low latitudes SPICAM also shows an ozone maximum around aphelion (although weaker than in the HST and Earth-based data) as well as substantial quantities between $L_s = 240\text{-}300^\circ$ likely associated with the southward transport of O₃-rich air masses from the northern polar vortex (Figure 13.10). Overall the O₃ at low-to-mid latitudes is not clearly anti-correlated to the amount of H₂O as measured by TES (Figures 13.1). Indeed, the variation in ozone is mainly caused by changes in the vertical distribution of H₂O rather than in the H₂O integrated column. As already mentioned in section 13.2, the wide vertical excursion of the H₂O saturation altitude over the martian year cause dramatic changes in the modeled HO_x content of the middle atmosphere (Figure 13.3). Around aphelion, the HO_x production is much reduced above the low hygropause and so is the O_x loss, as illustrated in Figure 13.9 where the photochemical lifetime of O_x at $L_s = 70^\circ$ reaches several hours to 1 day above 25 km. This leads to the build-up of a prominent seasonal O₃ layer above 25 km, first hypothesized by Clancy and Nair (1996) and reproduced by three-dimensional simulations (Lefèvre et al., 2004). Figure 13.8

shows however that the quantitative agreement with the O₃ observations at low latitudes is still imperfect. It is likely that a better match requires a very accurate description of the H₂O condensation and sedimentation processes around the hygropause level, which are difficult to represent in the models. With only a few uncertain O₃ profiles obtained at the same season ($L_s = 10-15^\circ$) from the Mars 5 (Krasnopolsky and Parshev, 1979) and Phobos 2 (Blamont and Chassefière, 1993) spacecraft, the modeled evolution of O₃ at low-to-middle latitudes could not be proved until the extensive O₃ profiling campaign by SPICAM provided a clear validation of the proposed mechanism (Lebonnois et al., 2006). Using the technique of stellar occultation, the instrument confirmed the presence of the ozone layer predicted by models between 25-50 km but essentially limited to the season $L_s = 30-110^\circ$ bracketing the Mars aphelion (Figure 13.13). Outside of this period, no ozone is found in the altitude range ($z > 20$ km) probed by the SPICAM instrument, meaning that the ozone detected in nadir viewing is confined near the surface.

The photochemistry of oxygen on Mars can also be investigated by the observation of the dayglow emitted at 1.27 μm by O₂ in its excited state O₂(¹ Δ_g). This dayglow was discovered on Mars by Noxon et al. (1976) and observed in three latitude bands by Traub et al. (1979). The dayglow is excited by photolysis of O₃ in (26) with a yield of O₂(¹ Δ_g) close to one. The deactivation of the excited O₂(¹ Δ_g) molecule towards the ground electronic state O₂(X³ Σ_g) occurs by emission of a photon at 1.27 μm with a relaxation time of ~ 1.2 h:



At low altitudes (i.e., large densities), deactivation of O₂(¹ Δ_g) also occurs by collision with CO₂:



The rate constant of this quenching by CO_2 is currently only constrained by an upper limit equal to $2 \times 10^{-20} \text{ cm}^3 \text{ s}^{-1}$ (Sander et al., 2011). Because $\text{O}_2(^1\Delta_g)$ is essentially produced by the O_3 photolysis, the dayglow intensity in (29) reflects the abundance of O_3 at the altitudes where the quenching in (30) plays a minor role. This altitude range is usually 20-40 km and is just that of the variations of the H_2O condensation level discussed in 13.2, which makes the $\text{O}_2(^1\Delta_g)$ dayglow a sensitive tracer of the interactions between the oxygen and hydrogen species. Using a long-slit high-resolution spectrograph, Krasnopolsky (1997) initiated a long-term ground-based campaign of mapping observations of the $\text{O}_2(^1\Delta_g)$ dayglow (Krasnopolsky and Bjoraker 2000; Novak et al. 2002; Krasnopolsky, 2003b, 2007, 2013). At low latitudes, the measurements show a decreasing $\text{O}_2(^1\Delta_g)$ dayglow from ~ 6 Mega-Rayleigh (MR) near aphelion to ~ 1 MR near perihelion, whereas the dayglow in the subpolar regions is highly variable with intensities up to 20 MR. Since the arrival of Mars Express at Mars in 2004, the infrared channel of SPICAM has provided the first continuous monitoring of the $\text{O}_2(^1\Delta_g)$ dayglow (Fedorova et al., 2006). The 2004-2012 average of the SPICAM observations in Figure 13.14 shows an obvious correlation with the O_3 observations by the same instrument in Figure 13.10. The brightest airglow is observed in the sunlit portions of the winter polar vortices, where the O_3 is usually located near the surface but in quantities so large that the radiative deactivation of $\text{O}_2(^1\Delta_g)$ can outweigh the effect of quenching by CO_2 . At low latitudes, the maximum $\text{O}_2(^1\Delta_g)$ emission around aphelion is clearly visible and is caused by the photolysis of the seasonal maximum of O_3 observed above the hygropause. The comparison of the SPICAM observations with the Earth-based measurements of Krasnopolsky (2003b) shows a very good agreement if one takes into account

the difference in the local time of the observations. Other observations of the $\text{O}_2(^1\Delta_g)$ dayglow from Mars Express have been performed by Altieri et al. (2009) with the OMEGA instrument. Because of its mapping capabilities, OMEGA has provided the first snapshots of the $\text{O}_2(^1\Delta_g)$ latitude-longitude distribution. The observations show an emission of up to 30 MR at high southern latitudes, with a clear maximum around local noon. This very bright $\text{O}_2(^1\Delta_g)$ dayglow can only result from the photolysis of large amounts of O_3 and is therefore consistent with direct observations of O_3 and chemical models which all indicate the presence of strong O_3 maxima in the dry winter polar vortices.

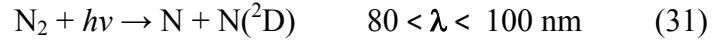
Another pathway to form $\text{O}_2(^1\Delta_g)$ is the termolecular association of O atoms by reaction (4). Indeed, this reaction produces O_2 in several excited states, which leads ultimately to the production of $\text{O}_2(^1\Delta_g)$ with a quantum yield estimated to 0.7-0.75 on Mars and Venus (Crisp et al., 1996; Krasnopolsky, 2011). The emission at 1.27 μm that follows has been observed for a long time on the night side of Venus (e.g., Connes et al., 1979; Gérard et al., 2009). On Mars, the $\text{O}_2(^1\Delta_g)$ emission at 1.27 μm caused by the association of O atoms can also be searched for at night, when the $\text{O}_2(^1\Delta_g)$ emission triggered by the ozone photolysis is shut off. The first detections of the $\text{O}_2(^1\Delta_g)$ nightglow on Mars were recently reported from the observations of the OMEGA (Bertaux et al., 2012), SPICAM (Fedorova et al., 2012) and CRISM (Clancy et al., 2012; 2013b) spectrometers on Mars Express and MRO. All instruments show that the $\text{O}_2(^1\Delta_g)$ nightglow at 1.27 μm is a quasi-permanent feature of latitudes beyond 70° in winter that occurs in a distinct layer located at 40-60 km altitude in the polar night region (Figure 13.15). Once integrated vertically, the nighttime $\text{O}_2(^1\Delta_g)$ emission caused by the reaction $\text{O} + \text{O} + \text{M}$ is about one order of magnitude weaker (0.1-0.4 MR) than the typical values of the daytime $\text{O}_2(^1\Delta_g)$ emission caused by O_3 photolysis. Three-dimensional models show that the martian $\text{O}_2(^1\Delta_g)$

nightglow is a direct consequence of the polar convergent flow associated with the strong wintertime Hadley circulation (Figure 13.16). Above the winter pole, the O atoms produced at high altitudes and solar illuminated latitudes are transported by the downwelling branch of the Hadley cell until the density is large enough to trigger the three-body reaction (4) and the subsequent $\text{O}_2(^1\Delta_g)$ nightglow at $1.27\text{ }\mu\text{m}$. This process continues until complete exhaustion of O atoms at lower altitudes, which explains why the emission is confined to a relatively narrow altitude layer. Near equinox, the $\text{O}_2(^1\Delta_g)$ nightglow can even be observed simultaneously over both polar regions, when the Hadley circulation splits into two branches and a downward transport of O atoms occurs over high latitudes of both hemispheres (Clancy et al., 2012; 2013b). Three-dimensional simulations of the LMD GCM show that the mechanisms leading to the $\text{O}_2(^1\Delta_g)$ nightglow can be well reproduced near solstice and equinox, but the model tends to overestimate the emission by 25% and the modeled seasonal variations between these two periods are still poorly simulated (Clancy et al., 2012). These problems reflect an inaccurate description of the polar night upper atmosphere circulation which is notoriously difficult to reproduce precisely in three-dimensional models, and for which observations of tracers like nighttime $\text{O}_2(^1\Delta_g)$ provide powerful constraints.

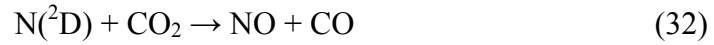
13.4 NITROGEN CHEMISTRY

The presence of molecular nitrogen in the atmosphere of Mars was discovered in 1976 by the Viking experiments (Nier et al., 1976; Owen et al., 1977), which determined a mixing ratio of 0.027 for N_2 . This figure remained unchallenged until the SAM suite on Curiosity recently revealed a mixing ratio of 0.0189 for N_2 (Mahaffy et al., 2013). This 30% smaller proportion of N_2 is believed to be more accurate than the previous Viking determination and will have to be

taken into account in future model simulations. However, the strong N-N bond makes N₂ a relatively inert species. Breaking of this bond and activation of nitrogen chemistry occurs at high altitude ($z > 120$ km) in the Mars atmosphere by photon and electron impact dissociation, as well as by a few ionospheric reactions not detailed here. Dissociation of N₂ in the extreme ultraviolet leads to the formation of atomic nitrogen in the ground state and in the metastable state N(²D):



The N(²D) atoms are quenched by O and CO or react with CO₂ to form NO:



Energetic electrons formed by photoionization of CO₂, N₂, O, and CO contribute to N production at high altitude via:



Thus, the odd nitrogen species N and NO are the main products of nitrogen chemistry in the upper atmosphere. At night, the reaction between N and O may excite the ultraviolet nightglow of the NO γ and δ bands, as observed by SPICAM (Bertaux et al., 2005):



During the day, NO is removed by predissociation in the $\delta(0-0)$ and $(1-0)$ bands at 190 and 182 nm:



The sink of odd nitrogen produced in reactions (31) and (33) is the recombination by:



If the production of N in the upper atmosphere is larger than that of NO, then the downward flux of odd nitrogen mainly consists of N atoms. In the lower atmosphere, a rapid loss process of N is:



This reaction is followed by (36), which altogether limit N and NO to small amounts by returning them to the stable species N_2 . If the downward flux of NO is greater than that of N, then the excess of NO initiates a more complicated chemistry (Yung et al., 1977; Krasnopolsky, 1993, 1995; Nair et al., 1994) and NO can persist in larger amounts in the lower atmosphere where its photolysis in (35) is slow. In these conditions an important reaction becomes:

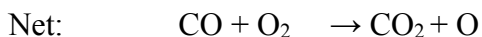


This reaction efficiently converts HO₂ into one hydroxyl radical OH available to oxidize CO by reaction (12). In addition, it causes the breaking of the O-O bond and the subsequent release of O through the rapid photolysis of NO₂ at visible wavelengths:

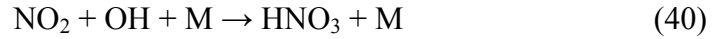


The above reactions (38-39) introduce the following cycle, which illustrates the possible coupling between the nitrogen, hydrogen, and oxygen chemistries in the Mars lower atmosphere:

Cycle III



As for cycles I and II, the net effect of this cycle is the reformation of CO₂ from CO but here both HO_x and nitrogen oxides NO_x (NO and NO₂) are used as catalysts. Model studies estimate the contribution of cycle III to the total production of CO₂ to be 5-10% (Nair et al., 1994; Yung et DeMore, 1999; Krasnopolsky, 2010). Another consequence of cycle III is the formation of O atoms, which facilitates the production of ozone. This is a well-known effect of this cycle in the polluted troposphere on Earth. The termination of cycle III occurs when NO₂ returns to a more stable form of nitrogen such as nitric acid HNO₃ or peroxyntic acid HO₂NO₂:



HNO_3 and HO_2NO_2 are however photolyzed more rapidly on Mars than they are on Earth, and consequently play a lesser role as reservoirs of NO_x . For a total NO_x amount of 0.6 ppbv in the first scale height above the surface, one-dimensional models predict a mixing ratio of the order of 1 pptv for HNO_3 and of 10 pptv for HO_2NO_2 (e.g., Yung et al., 1999).

As mentioned above, the overall importance of the nitrogen chemistry in the Mars lower atmosphere depends on a fine balance between the production of N and NO in the thermosphere, whose kinetics is not known within the required accuracy (Nair et al., 1994; Krasnopolsky, 1995). NO was detected down to 120 km by the Viking mass spectrometers (Nier and McElroy, 1977), which suggests a downward flow of NO. However, the rather bright NO nightglow observed by SPICAM (Bertaux et al., 2005; Cox et al., 2008) in the flow descending to the middle atmosphere (60-80 km) suggests that N is more abundant than NO in the thermosphere. At night, the airglow produced in reaction (34) is immediately followed by the recombination of odd nitrogen in (36), which prevents the supply of NO to the lower atmosphere. Up to now the only attempt to detect NO in the lower atmosphere was made using its strongest absorption lines at 5.3 μm and resulted in an upper limit of 1.7 ppbv (Krasnopolsky, 2006b). The nitrogen chemistry on Mars is therefore poorly constrained by observational data. In any case, a precise estimation of its importance requires better kinetics data, models extending up to the region of production of odd nitrogen ($z > 150$ km), and a good representation of transport from the thermosphere down to the lower atmosphere. This latter point can be better accomplished with a

general circulation model with full nitrogen chemistry. Up to now the only simulation of this kind was performed by Moudden and McConnell (2007), who obtained ~ 0.4 ppbv of NO_x in the lowest 20 km (Figure 13.17). This number is close to the ~ 0.6 ppbv previously obtained with one-dimensional models (Nair et al., 1994; Krasnopolsky, 1995).

13.5 SULFUR AND CHLORINE CHEMISTRY

On Earth, sulfur dioxide SO_2 is the most abundant species outgassed by volcanoes after CO_2 and H_2O . Although there is no evidence of active volcanism on Mars today, localized outgassing sources cannot be excluded, and the presence of SO_2 in the atmosphere might be indicative of such activity. However, despite many attempts SO_2 remains up to now undetectable on Mars. The two most recent searches for SO_2 , both performed from the Earth in the thermal infrared, are those of Encrenaz et al. (2011) and Krasnopolsky (2012), who both determined an upper limit of 0.3 ppbv. This value is well below the value of ~ 10 ppbv from which SO_2 can have a significant impact on the CO_2 chemical stability of Mars (Krasnopolsky, 1993). The influence of SO_2 on the martian photochemistry at the global scale is therefore negligible. Nevertheless, it is interesting to calculate the theoretical loss rate of SO_2 as it may be converted to a chemical lifetime and an upper limit on the production of SO_2 at the surface. Krasnopolsky (2005b) developed a 1D model of sulfur chemistry for that purpose. After release of SO_2 in the atmosphere, photochemical equilibrium is established between SO_2 and its photolysis products SO and S:



Photolysis in (42-43) does not constitute a net sink of SO₂ since S is rapidly reformed to SO:



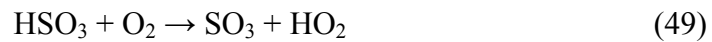
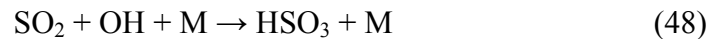
and SO₂ is recycled from SO by :



Reactions (45-47) maintain SO₂ as the dominant sulfur species up to ~45 km (Figure 13.18).

Above that level, their efficiency decreases and SO becomes the primary sulfur species.

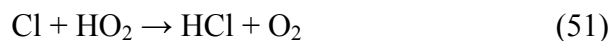
The irreversible loss of SO₂ occurs mainly through the reaction with OH, which initiates the following oxidation chain:



The end product of the chain, sulfuric acid H₂SO₄, can then either condense (Wong et al., 2003) or be trapped at the surface of water-ice aerosols (Krasnopolsky, 2005b). Thus the precipitation of a solid form of H₂SO₄ to the surface is the most likely removal process of sulfur in the Mars atmosphere. The SO₂ lifetime is determined by reaction (48). It was estimated by Krasnopolsky

(2005b) to be of the order of 2 terrestrial years, which results in an upper limit to the production of SO₂ of 17000 t y⁻¹ to sustain a globally-averaged mixing ratio of 1 ppbv. The new upper limit of 0.3 ppbv determined by Encrenaz et al. (2011) and Krasnopolsky (2012) implies that the maximum production of SO₂ must be reduced accordingly to about 5000 t y⁻¹, which is smaller than the volcanic source of SO₂ on Earth by a factor of ~1500 (Haywood and Boucher, 2000). This fact, along with the absence of any “hot spots” or endogenic heat sources in the THEMIS images (Christensen et al., 2003) suggests that outgassing at the surface of Mars must be very weak, if it exists at all. It is also noteworthy that SO₂ is a relatively long-lived species on Mars. This means that it can be transported by the winds far from its source and be diluted by atmospheric mixing. Thus, a possible detection of SO₂ in the future would be indicative of outgassing somewhere at the surface of the planet but not necessarily in the proximity of the region of detection.

In addition to sulfur, volcanic eruptions on Earth are capable of injecting large amounts of chlorine in the atmosphere, usually in the form of hydrochloric acid HCl. If present on Mars, HCl might therefore be indicative of some outgassing activity. The discovery of small amounts of perchlorate (ClO₄) in the martian soil by the Phoenix lander (Hecht et al., 2009) and the Curiosity rover (Glavin et al., 2013) also raises the possibility of chlorine delivered to the atmosphere by the surface or the airborne dust. Whatever the source is, HCl should be the dominant chlorine species on Mars since any Cl atom released in the lower atmosphere is rapidly converted to the stable species HCl by reaction with HO₂:



However, as for SO_2 , HCl has up to now never been detected in the Mars atmosphere. Recently the upper limit of 2 ppbv determined from the Earth by Krasnopolsky et al. (2007) was lowered to 0.2 ppbv from Herschel/HIFI submillimetric observations (Hartogh et al., 2010a). With this amount of HCl the predicted mixing ratio of Cl is less than 1 pptv in the lower atmosphere. The production of odd chlorine on Mars is therefore at least three orders of magnitude smaller than that of odd hydrogen. On the basis of the current data in hand, this makes chlorine a negligible contributor as a potential catalyst of martian atmospheric chemistry.

13.6 THE METHANE CONTROVERSY

Between 2004 and 2012, four independent teams reported detections of low levels (10-60 ppbv) of methane on Mars. If true, these would constitute the first observations of an organic compound on that planet and would be the main novelty of recent years in the inventory of minor species in its atmosphere. However, as we will show in the following, the claims for the presence of methane have been highly controversial over the last decade. Recently, the most robust search for methane was performed on the surface of Mars by the Tunable Laser Spectrometer (TLS) on Curiosity. The latest TLS measurements indicate a background CH_4 level of 0.7 ppbv and have identified a pulse of 7 ppbv only observed over a period of two months (Webster et al., 2015).

The first report of methane detection on Mars was by Krasnopolsky et al. (2004) who observed 10 ± 3 ppbv of methane in January 1999 at $L_S = 88^\circ$ using the Fourier Transform Spectrometer (FTS) at the Canada-France Hawaii Telescope. The field of view covered a significant part of the martian disk. The same year, Formisano et al. (2004) detected varying methane amounts between 0-30 ppbv over a few orbits of the PFS spectrometer on Mars Express. Geminale et al. (2011)

expanded on this using the same instrument and method over a six-year baseline. Their results revealed substantial seasonal variations of methane and local enhancements of up to 70 ppbv at high northern latitudes in summer. The global mean value derived from PFS is about 15 ppbv. Using the CSHELL spectrometer at the IRTF (Hawaii), Mumma et al. (2009) observed in January-March 2003 a strong local maximum (~ 50 ppbv) of methane at low latitudes over the Syrtis Major region (Figure 13.19). No significant levels of methane were found in their observations performed three years later in January-February 2006. Krasnopolsky (2012) reprocessed with a refined analysis his CSHELL observations of February 2006 at $L_s = 10^\circ$ and found about 10 ppbv of methane over the Valles Marineris region and ~ 3 ppbv outside this region. His observations in December 2009 at $L_s = 20^\circ$ and March 2010 at $L_s = 70^\circ$ showed no detection with an upper limit of 8 ppbv. Villanueva et al. (2013) also used the CSHELL spectrometer in January 2006 but only derived an upper limit of 7.8 ppbv, in contrast to the 10 ppbv detected by Krasnopolsky (2012) one month later. Villanueva et al. (2013) did not detect methane in their later observations of November 2009 and April 2010. All the above studies measured CH_4 in its absorption band at $3.3 \mu\text{m}$. Using the band at $8 \mu\text{m}$, Fonti and Marzo (2010) performed a statistical analysis of the Thermal Emission Spectrometer (TES) spectra and extracted a weak signal attributed to methane absorption and showing seasonally variable methane at the ~ 10 -30 ppbv level.

It is fair to say that the claimed detections of such low levels of methane were all obtained at the limits of the instrumental capabilities. PFS and TES spacecraft instruments do not have the required sensitivity and spectral resolution for an unambiguous identification of CH_4 (Zahnle et al., 2011). Detection of methane is made by summing thousands of spectra, which does not suppress –and can even increase– instrumental effects and systematic errors. Despite their much

greater spectral resolution, ground-based observations are not easier because the martian methane must be viewed through the Earth's atmosphere which contains $\sim 10^4$ more methane molecules above the observer than what is retrieved on Mars. The measurements must therefore exploit the Doppler shift of the martian lines when Mars is approaching or receding from Earth. However, even in these conditions, the claimed detections of methane are close to the noise level and may be sensitive to contamination by telluric absorption (Zahnle et al., 2011). In any case, the very different geographical distributions and seasonal variations of methane obtained from space (Geminale et al., 2011; Fonti and Marzo, 2010) and from the Earth (Mumma et al., 2009) are puzzling and cast doubt on their veracity.

Despite these reservations, the observational claims for methane on Mars between 1999 and 2006 naturally raise the question of sources and sinks. Regarding the source, methane is not produced photochemically. It is therefore tantalizing to relate its existence to a possible past or extant life on the planet, since more than 90% of methane on Earth has a biological origin). Krasnopolsky (2006c) calculated that methane from impacts of comets, meteorites, and interplanetary dust is insignificant and argued that the lack of volcanism, hot spots, and SO_2 (which is more abundant than CH_4 in terrestrial outgassing) favors the hypothesis of a biogenic origin for martian methane. On the other hand, Keppler et al. (2012) argued that carbonaceous micrometeorites might be in sufficient quantity on the surface of Mars to become a significant abiogenic source of methane when exposed to ultraviolet radiation. Alternatively, Atreya et al. (2007) proposed that methane could be produced abiogenically by hydrothermal processes such as serpentinization, i. e., the reaction between iron-bearing silicates and water, producing H_2 , which in turn reacts with CO_2 to form CH_4 . On Mars this would require however the existence of shallow aquifers and an active hydrogeochemistry, which have yet to be discovered.

Regarding the sink, the primary photochemical loss of methane occurs through its oxidation by OH or O(¹D), and its photolysis by the Lyman α line above ~80 km altitude. These processes lead to a global chemical lifetime estimated to 300-340 terrestrial years (Summers et al., 2002; Krasnopolsky, 2004; Lefèvre and Forget, 2009) to which corresponds a tiny source of 260 t yr⁻¹ to maintain a steady-state value of 10 ppbv. This may be compared with the terrestrial value of 582x10⁶ t yr⁻¹ (Solomon et al., 2007). With a lifetime of ~300 years, methane on Mars is expected to be homogeneously mixed by atmospheric transport. Lefèvre and Forget (2009) showed that reproducing the methane observations by Mumma et al. (2009) with a GCM requires a methane lifetime shorter than ~200 days, and hence an unknown sink that is at least 600 times faster than the loss derived from the current kinetics data used by the atmospheric chemistry community. The fact that such a strong oxidizing process would have been overlooked would be a surprise since conventional models do a rather good job at reproducing short-lived chemical species on Mars (e.g., O₃ and H₂O₂), as shown in previous sections.

Several studies explored the chemical or physical processes that could explain a fast methane loss but none of them is supported by current laboratory data. For instance, methane could be destroyed by electrochemical processes triggered by the strong electric fields generated during dust storms (DeLory et al., 2006; Farrell et al., 2006). A large-scale electrochemical production of oxidants in the atmosphere is disputed by the calculations of Krasnopolsky (2006a) and seems difficult to reconcile with current observations of H₂O₂, O₃ and CO (Lefèvre and Forget, 2009). However, locally the excess of H₂O₂ produced in dust storms could lead to its precipitation out of the atmosphere onto the martian surface (Atreya et al., 2006, 2007). Methane would then be scavenged by large amounts of H₂O₂ or other superoxides embedded in the regolith. This

possibility is for the moment not supported by laboratory work, which shows no apparent oxidation of methane with H_2O_2 on analogs of martian soil or perchlorates (Gough et al., 2011). In addition, kinetic data on reactions of CH_4 with metal oxides and superoxides ions are extremely slow at martian temperatures (Krasnopolsky, 2006c). Laboratory work also shows that wind-driven agitation of quartz crystals could produce active sites that sequester methane (Knak Jensen et al., 2014), but it is difficult to extrapolate the efficiency of these highly idealized experiments to the real martian atmosphere. Another speculative possibility is that the decomposition of methane condensed as clathrates would be a source of episodic release of CH_4 (e.g., Chastain and Chevrier, 2007; Chassefière, 2009). However this does not solve the problem of the methane sink (Zahnle et al., 2011). According to laboratory work (Trainer et al., 2010), trapping of CH_4 on polar ice analogs (including clathrates) appears anyway to be negligible in the modern martian conditions.

Because of the potential implications of the presence of methane and in the light of the controversial observational dataset described above, the first in-situ measurements promised by TLS on Curiosity and its far superior detection capabilities have been eagerly awaited. The first atmospheric samples collected by TLS in the Gale crater (4°S , 137°E) spanned a 8-month period in spring-summer. By combining all of the individual measurements it was concluded that methane was not detected having an upper limit of only 1.3 ppbv (Webster et al., 2013). In a subsequent analysis, Webster et al. (2015) presented the entire TLS dataset reprocessed over a period of almost one martian year (605 sols). The results indicate detection of methane at two levels of abundance (Figure 13.20). A background CH_4 level of 0.7 ± 0.2 ppbv, based on high-precision methane-enriched experiments, is observed during the first 8 months and last 4 months

of the dataset. Between these two periods, four sequential measurements of TLS indicate a pulse of 7 ± 2 ppbv of methane over two months ($L_s = 56\text{-}82^\circ$). If true, these results raise a number of questions that currently have no answer. First, the only way to reconcile the last Earth-based reports of methane (2003-2006) and the low background level initially measured by Curiosity would be a near-complete disappearance of methane in less than 10 years. There is currently no confirmed mechanism that could explain a loss of methane that is in such stark contradiction with its theoretical 300-year lifetime. Then, it is difficult to conceive a release process that is sufficiently restricted in time to explain the methane pulse detected by TLS. For instance, both serpentinization (occurring a few kilometers below the surface) and the action of ultraviolet on organics (widespread on the surface) are slow and continuous processes that have in principle no preferred particular time. Even in the case of episodic methane release, transport and mixing by the winds would also rapidly smooth out any plume of methane emitted by a localized source, unless that emission occurred very close to Curiosity. Because it challenges so much our current understanding of the atmospheric chemistry and physics on Mars, the discovery of variable amounts of methane by TLS will probably have to be confirmed by further detections to rule out any possible sources of error and fully convince the scientific community. Future searches for methane by Curiosity and the Trace Gas Orbiter are therefore a high priority to unravel a mystery that may impact Mars science in a fundamental way.

13.7 RECONCILING OBSERVATIONS AND MODELS

13.7.1 One-dimensional annually-averaged models

As for the Earth atmosphere, photochemical models are essential tools for understanding the composition and chemical processes at work in the martian atmosphere. One-dimensional globally-averaged models were especially important when observational data were scarce and global climate models (GCM) did not exist. Their first major success was the demonstration of the catalytic effect of the hydrogen chemistry by McElroy and Donahue (1972) and Parkinson and Hunten (1972), who could provide a qualitative explanation for the surprisingly low amounts of observed CO and O₂ on Mars. After four decades of progress and many new observational constraints, this initial discovery has never been called into question. However, our quantitative understanding of the long-lived chemical species on Mars remains poor. In particular, the observed equilibrium value of CO (900-1100 ppmv) has been historically difficult to reproduce and this issue has still not been solved in current long-term simulations of the martian photochemistry.

It was assumed in the early 1970s that martian atmospheric temperatures decreased with height with a steep gradient of $-5^{\circ} \text{ K km}^{-1}$ down to 150 K above 15 km. In these conditions water vapor was restricted to the first 5 km above the surface and photochemical models tended to produce too little HO_x, which led to large CO amounts relative to the observations. To counteract this effect, models adopted unrealistically large H₂O₂ amounts (Parkinson and Hunten, 1972) or very strong eddy mixing coefficients (McElroy and Donahue, 1972; Liu and Donahue, 1976; Kong and McElroy, 1977a) to speed up CO oxidation and reform CO₂ fast enough in the simulations. Later, it was recognized that the room temperature value of the CO₂ absorption cross-section had to be reduced under martian conditions to account for its temperature dependence (Lewis and Carver, 1983; Anbar et al., 1993a). This has the effect of increasing the amount of ultraviolet radiation available to photodissociate water vapor, creating the opposite problem of an

overproduction of HO_x and too little CO in the models. With temperature-dependent CO_2 cross-sections and the standard kinetics, the typical CO mixing ratio calculated by current one-dimensional models is 120 ppmv (Nair et al., 1994; Krasnopolsky, 2010), which is about 8 times smaller than the observed value of 900-1100 ppmv (section 13.2). Figure 13.21 provides an example of the photochemical composition calculated by such models (Krasnopolsky, 2010). The abundance of short-lived species (O_3 , $\text{O}_2(^1\Delta_g)$, H_2O_2) is in good agreement with the observations, but this success still relies on a CO amount that is largely underestimated (120 ppmv). To solve the general issue of CO in globally-averaged models, Nair et al. (1994) modified the rates of the key reactions $\text{CO} + \text{OH}$ and $\text{HO}_2 + \text{OH}$ within their experimental uncertainties and reached ~ 500 ppmv of CO in their model. However, subsequent laboratory studies and stratospheric measurements on Earth have not supported the suggested modifications. Krasnopolsky (1995) in turn proposed to decrease the efficiency of the HO_x chemistry by reducing the H_2O photolysis by a factor of two to account for uncertainties in the measured H_2O absorption cross-sections, and obtained a CO abundance of ~ 500 ppmv. Water vapor is indeed essentially photolyzed in the narrow interval 190-200 nm where its absorption cross-section was not at that time well constrained by measurements, especially at low temperatures. The later laboratory data by Chung et al. (2001) indicated a moderate decrease ($\sim 20\%$) with temperature of the H_2O cross-section between 295 K and 250 K and 187-189 nm. Unfortunately, measurements at temperatures more representative of the altitudes at which H_2O is photolyzed ($T < 200$ K) are still missing.

The above models only consider gas-phase chemistry. On Earth, heterogeneous reactions between gaseous species and solid particles (such as ice or mineral dust) also play an important role in controlling the composition of the atmosphere and are a standard feature in most

photochemical models. In view of the ubiquity of water-ice clouds and dust in the atmosphere of Mars, there are good reasons to examine the possibility of heterogeneous processes also active on that planet. The reactions that have received particular interest on Mars are the interactions between gaseous OH, HO₂, H₂O₂ and water-ice and dust particles, since they may provide a sink for HO_x and contribute to throttle down the recycling rate of CO₂ from CO. In order to have an effect on the HO_x budget the uptake of these species on the solid phase must be irreversible (i.e., reactive) or, if reversible, must be sufficiently strong to lead to a significant removal from the gas phase. The irreversible losses of OH and HO₂ on water-ice have been identified in the laboratory, with reaction probabilities are ~0.03 and ~0.025, respectively (Cooper and Abbatt, 1996). The uptake of H₂O₂ on water-ice is reversible and the partitioning coefficient between the gas and solid phases is still uncertain (Crowley et al., 2010). By analogy with what occurs on mineral dust surfaces on Earth, the uptake of HO_x or other species on martian dust may also be important. However, in the absence of real samples, the uptake coefficients derived on terrestrial dust particles are still highly speculative when applied to Mars. Kong and McElroy (1977a) made the first attempt to consider quantitatively the heterogeneous destruction of HO_x, but only took into account the adsorption on the regolith at the martian surface. With more comprehensive 1D models including gas-surface interactions on water-ice clouds and airborne dust, Anbar et al. (1993b) demonstrated the potential importance of heterogeneous chemistry in lowering the abundance of HO_x, while Krasnopolsky (1993) noted a doubling of CO in his model that led to improved agreement with the observations. Both authors emphasized, however, the lack of observational constraints on critical parameters such as the HO_x reaction probabilities on dust and ice, which were largely unknown at that time, or the altitude distribution of the cloud and dust particles. In a more recent study, Krasnopolsky (2006a) investigated the impact of heterogeneous chemistry with an updated kinetics and ice vertical distribution. He showed that it

was possible to fit the observed CO only on the condition that the probabilities for heterogeneous loss of HO_x on ice are 4-30 times larger than those currently recommended for atmospheric modeling on Earth (Sander et al., 2011). In addition, the seasonal-latitudinal variations of O₃, O₂(¹Δ_g), and H₂O₂ calculated with the same extreme heterogeneous parameters strongly disagree with the observations, which is problematic. This result suggests that heterogeneous chemistry is not a simple and unique solution to the low CO amounts predicted by martian photochemical models. An alternative way to decrease oxidizing species (and hence to increase CO) may be to consider their dry deposition at the surface, as done for O₃ and H₂O₂ in the 1D model of Zahnle et al. (2008). With this assumption, their model could reach a CO value of 470 ppmv. This is larger than the typical value produced by 1D gas-phase models but is still underestimated by a factor of two relative to the observations. Even with the inclusion of dry deposition, it is only at the cost of extreme conditions of dryness throughout the atmosphere and the martian year that Zahnle et al. (2008) could reach a CO value of 750 ppmv in reasonable agreement with the observed CO.

All the above calculations are based on annually- and globally-averaged models. These models are very useful to estimate the first-order distribution of chemical species as a function of height and are the only tools available to examine the fate of the long-lived species which require simulations of several decades (for CO and O₂) to thousands of years (for H₂) before reaching equilibrium. A basic problem of globally-averaged models, however, is their inability to represent the dramatic latitudinal and vertical variations of water vapor over the martian year, which are now well documented by satellite observations (Figure 13.1). Since H₂O is the main source of HO_x species, the oxidation rate of CO and reformation rate of CO₂ obviously experience very large variations in time and space over the martian year that cannot be easily

represented in an annually, globally averaged sense. In addition, averaged models cannot account properly for the large observed variations in temperature, water-ice, and dust, for which the response in terms of gas-phase kinetics and heterogeneous chemistry is known to be highly non-linear.

13.7.2 One-dimensional time-dependent models

A first step in developing more complex models that avoid the problems mentioned above is to constrain the existing 1D models with varying profiles of temperature and water vapor. By nature this approach can only represent local conditions and still neglects the changes due to horizontal transport. Time-dependent 1D models are, however, very convenient to study the fast chemistry by simulating the distribution of short-lived species that respond quickly to the local abundance of H₂O. Owing to its short lifetime (see section 13.3), ozone is obviously a good candidate: this was recognized by Shimazaki (1981) who used a uniform but seasonally-varying profile of water vapor constrained by Viking data to reproduce with some success the Mariner 9 observations of high-latitude ozone. Clancy and Nair (1996) calculated the seasonal changes in photochemistry using seasonally-varying water vapor profiles constrained from direct observations or temperature profiling (Clancy et al., 1996). They could predict a large decrease in the low-latitude O₃ amount between aphelion and perihelion, a trend that was confirmed several years later by O₂(¹Δ_g) Earth-based observations (Krasnopolsky, 2003b) and by the SPICAM nighttime O₃ measurements (Lebonnois et al., 2006; Figure 13.13). However, the CO mixing ratio obtained in their simulation was still largely underestimated and only 16% larger than that calculated without seasonal variations of temperature and H₂O (Nair et al., 1994). More recently, Krasnopolsky (2006, 2009) modeled the seasonal and altitudinal variations of the

photochemistry with a 1D model using constant values of the long-lived species CO, O₂, H₂ as constrained by observations, whereas the seasonal evolution of H₂O, water-ice clouds, and dust amount was adjusted to the TES observations (Smith, 2004). This study took advantage of the much improved observational dataset of short-lived species in recent years to investigate the latitudinal-seasonal evolution of O₃, H₂O₂, and O₂(¹Δ_g). Figure 13.22 displays the results of these 1D simulations carried out for ~100 seasonal-latitudinal points. It shows that good agreement between modeled and observed ozone can be obtained in the tropics and midlatitudes provided that the long-lived species and H₂O are maintained in the model to their observed values (some results for H₂O₂ are shown in Figure 13.7). The model cannot accurately represent trace gases when the effects of transport become important as is the case in the polar night or at high latitudes in winter, where O₃ is underestimated (Figure 13.22).

One-dimensional time-dependent models have also been used to study the variations of martian chemical species with local time (Krasitski, 1978; Shimazaki, 1981; García Muñoz et al., 2005; Krasnopolsky, 2006a). García Muñoz et al. (2005) examined the diurnal cycle of the emissions of O₂(¹Δ_g) and of the vibrationally excited levels of OH. During the day, the peak of the O₂(¹Δ_g) dayglow produced by the O₃ photolysis (reaction 26) occurs shortly after noon in their model, in rather good agreement with the Earth-based observations (Krasnopolsky, 2003b) and the O₂(¹Δ_g) images obtained from OMEGA (Altieri et al., 2009). At this time of the day, their modeled intensities are 0.55 MR or 0.95 MR depending on the value adopted for the quenching rate of O₂(¹Δ_g) in (26), taken as $k_{\text{CO}_2} = 2 \times 10^{-20} \text{ cm}^3 \text{ s}^{-1}$ or $k_{\text{CO}_2} = 1 \times 10^{-20} \text{ cm}^3 \text{ s}^{-1}$, respectively. These intensities calculated at 20°N are rather low compared those observed from Mars Express (Figure 13.14) and by Krasnopolsky (2013). A similar study was performed by Krasnopolsky (2006a) for $L_s = 112^\circ$ and 173° at the subsolar latitudes of 22°N and 3°N respectively, who used

the profiles of temperature, water vapor, and dust measured in the same conditions by TES (Smith, 2004). With these constraints the calculated values of the $\text{O}_2(^1\Delta_g)$ dayglow at $1.27\ \mu\text{m}$ (Figure 13.25) are significantly larger than in García Muñoz et al. (2005) and in rather good agreement with the observations. At $L_s = 112^\circ$, the model predicted the nighttime ozone layer observed in this season by SPICAM (Figure 13.13), which results from the absence of photolysis and the rapid conversion of O atoms to O_3 by reaction (24) at dusk. These results were obtained with the same assumptions regarding the heterogeneous loss of H_2O_2 as mentioned above for Krasnopolsky (2009). García Muñoz et al. (2005) and Krasnopolsky (2006a) also examined the emission of $\text{O}_2(^1\Delta_g)$ produced at night. As mentioned earlier the main source of O_2 excitation in these conditions is the termolecular association of oxygen atoms in reaction (4). Both studies reported a nighttime emission of 10-30 kR at low latitude, in agreement with the upper limit of 40 kR derived by Krasnopolsky (2013) and weaker by an order of magnitude than the polar $\text{O}_2(^1\Delta_g)$ nightglow detected by OMEGA (Bertaux et al., 2012), SPICAM (Fedorova et al., 2012), and CRISM (Clancy et al., 2012).

13.7.3 Multidimensional models

With the sizeable increase in the observational dataset of atmospheric constituents obtained in the last decade, multi-dimensional models become essential tools for interpreting the interactions between chemistry and transport in all the environmental conditions (e.g., L_s , season, local time, dust, clouds) for which measurements are now available. The first three-dimensional model that included a simple chemistry (CO_2 photolysis and O recombination) was the Mars thermospheric GCM developed by Bougher et al. (1990) but its lower boundary was at $\sim 100\ \text{km}$. Moreau et al. (1991) then studied the meridional distribution of chemical species down to the surface with a

two-dimensional (zonally-averaged) model using a simplified water vapor field and dynamics. It is only recently that the increase in computer power allowed the development of full general circulation models (GCM) of Mars with photochemistry, similar to those commonly used for the study of the Earth atmospheric chemistry. In addition to an adequate representation of atmospheric transport, martian GCMs are able to provide a realistic description of the three-dimensional field of water vapor and its variations at all scales, which is a crucial advantage for constraining properly the fast chemistry of the lower atmosphere. A drawback is that the long computation times restrict 3D chemical simulations to 2-3 martian years. This duration is sufficient to investigate the fast chemistry of O_3 , H_2O_2 , or $\text{O}_2(^1\Delta_g)$, but is not long enough to examine the evolution of long-lived species (CO , O_2 , H_2), which are usually initialized to their observed value. Lefèvre et al. (2004) coupled a photochemical module to the LMD general circulation model and characterized the three-dimensional variations of ozone in the atmosphere of Mars. Their model could reproduce successfully the Mariner observations of O_3 but showed a significant underestimation of the O_3 maximum observed at low latitudes in the aphelion season (section 13.3). This issue noted with a pure gas-phase chemical scheme was later confirmed by a stringent comparison between the same LMD GCM and the complete SPICAM dataset of ozone (Lefèvre et al., 2008). In their study, Lefèvre et al. (2008) demonstrated that GCM simulations that include the recommended HO_x uptake on water-ice clouds could lead to much improved quantitative agreement with ozone measurements without violating current laboratory constraints (Figure 13.24). At the same time, the outstanding disagreement between the modeled H_2O_2 and the low upper limit observed by Encrenaz et al. (2002) around aphelion was reduced, allowing a better quantitative agreement with the H_2O_2 dataset throughout the martian year (Figure 13.7). Despite these improvements, the latest version of the LMD GCM in Figure 13.10 still tends to underestimate the low latitude O_3 column when compared to the SPICAM observations around

aphelion. This problem reflects more difficulties of GCMs in reproducing precisely the effect of the aphelion cloud belt on the water vapor vertical profile, than a gap in our understanding of the photochemistry. The same pattern is observed in the comparison between the LMD GCM and the $\text{O}_2(^1\Delta_g)$ dayglow observations (Figure 13.14). This is expected since the source of the $\text{O}_2(^1\Delta_g)$ dayglow is the O_3 photolysis, but this also underlines the good consistency of the SPICAM data obtained in two different wavelength ranges. As in Krasnopolsky (2009), the uncertain quenching rate of $\text{O}_2(^1\Delta_g)$ in (30) had to be reduced in the LMD GCM to $5 \times 10^{-21} \text{ cm}^3 \text{ s}^{-1}$ to agree with SPICAM at high latitudes, but remains consistent with the currently recommended upper limit of $2 \times 10^{-20} \text{ cm}^3 \text{ s}^{-1}$ (Sander et al., 2011).

A three-dimensional study was also presented by Moudden and McConnell (2007) who added a chemistry module to the 3D Mars Global Multiscale Model (GM3). A notable feature of their model is the comprehensive description of the nitrogen chemistry illustrated in Figure 13.17. The seasonal evolution of ozone given by GM3 agrees qualitatively with the observations considered in their study, and is consistent with the results of the LMD GCM. The quantitative analysis reveals, however, an overestimation of ozone in the perihelion season, which can probably be attributed to the constant dust optical depth of 0.5 used in GM3, leading to too cold and dry conditions for that period. Moudden (2007) also used GM3 to characterize the three-dimensional evolution of H_2O_2 and showed the extreme variations of this compound at high latitudes related to those of H_2O . At low-to-mid latitudes, the H_2O_2 columns calculated by Moudden (2007) (Figure 13.25) are in reasonable agreement with the current observations (Figure 13.7).

In recent years three-dimensional models have been increasingly used to analyze the measurements of the reactive species O_3 , $\text{O}_2(^1\Delta_g)$, or H_2O_2 . In such simulations the short-lived chemical species are discussed against a background of long-lived species CO , H_2 or O_2 that is

usually set to its observed value. Under these conditions, current 3D models indicate that the fast chemistry on Mars can be rather well reproduced quantitatively with the standard set of gas-phase and heterogeneous reactions used for terrestrial studies. However, this first step towards a global quantitative understanding of martian photochemistry should be strengthened by a better knowledge of some critical parameters. The precise amount of water vapor present in the middle and upper atmosphere is still insufficiently known due to the lack of observational data, but also because of the inevitable simplification of microphysical processes leading to water-ice condensation and sedimentation in models. New laboratory data are also needed to reduce the uncertainties on some important reactions governing the chemistry of HO_x radicals, on the possible heterogeneous reactions on martian solid surfaces, or on the temperature dependence of the CO_2 absorption cross-section below 200 K and that of H_2O below 250 K.

Because of the needed computation time, a current limitation of 3D models is that they have not been integrated over sufficiently long periods to investigate the long-term equilibrium value of the slow-evolving species CO , O_2 , or H_2 . Therefore, the significant underestimation of martian CO predicted by 1D globally averaged models is still an outstanding issue, and the classical problem of the Mars photochemical stability cannot therefore be considered fully understood. With the increase in computer power it is obvious that 3D models, which are the best-suited tools to reproduce the interactions between chemistry and transport on long timescales, will soon address this challenge.

13.8 REFERENCES

- Altieri, F., Zasova, L., D'Aversa, E., *et al.* (2009) O₂ 1.27 μm emission maps as derived from OMEGA/MEx data, *Icarus*, **204**, 499-511.
- Anbar, A. D., Allen, M., and Nair, H. A. (1993b) Photodissociation in the atmosphere of Mars: Impact of high-resolution temperature-dependent CO₂ cross-section measurements, *J. Geophys. Res.*, **98**, 10925– 10931.
- Anbar, A. D., Leu, M. T., Nair, H. A., *et al.* (1993b) Adsorption of HO_x on aerosol surfaces: Implications for the atmosphere of Mars, *J. Geophys. Res.*, **98**, 10933–10940.
- Anderson, D. E., and Hord, C. W. (1971) Mariner 6 and 7 ultraviolet spectrometer experiment: Analysis of hydrogen Lyman alpha data, *J. Geophys. Res.*, **76**, 6666-6671.
- Anderson, D. E. (1974) Mariner 6, 7, and 9 ultraviolet spectrometer experiment: analysis of hydrogen Lyman-alpha data, *J. Geophys. Res.*, **79**, 1513-1518.
- Atreya, S. K., Mahaffy, P. R., and Wong, A. S. (2007) Methane and related trace species on Mars : Origin, loss, implications for life and habitability, *Planet. Space Sci.*, **55**, 358-69.
- Atreya, S. K., Witasse, O., V.Chevrier, V. F., *et al.* (2011) Methane on Mars : Current observations, interpretation, and future plans, *Planet. Space Sci.*, **59**, 133-136.

- Barker, E. S. (1972) Detection of molecular oxygen in the martian atmosphere, *Nature*, **238**, 447-448.
- Barth, C. A., and Hord, C. W. (1971) Mariner 6 and 7 ultraviolet spectrometer experiment: topography and polar cap, *Science*, **173**, 197-201.
- Barth, C. A., C. Hord, C. W., Stewart, A. I., *et al.* (1973) Mariner 9 ultraviolet spectrometer experiment: seasonal variation of ozone on Mars, *Science*, **179**, 795-796.
- Bates, D. R., and Nicolet, M. (1950) The photochemistry of atmospheric water vapor, *J. Geophys. Res.*, **55**, 301-327.
- Belton, M. J. S., and Hunten, D. M. (1966) The abundance and temperature of CO₂ in the martian atmosphere, *Astrophys. J.*, **145**, 454-467.
- Bertaux, J. L., Leblanc, F., Perrier, S., *et al.* (2005) Nightglow in the upper atmosphere of Mars and implications for atmospheric transport, *Science*, **307**, 567-569.
- Bertaux, J. L., Gondet, B., Lefèvre, F., *et al.* (2012) First detection of O₂ 1.27 μ m nightglow emission at Mars with OMEGA/MEX and comparison with general circulation model predictions, *J. Geophys. Res.*, **117**, doi:10.1029/2011JE003890.

- Biemann, K., Owen, T., Rushneck, D. R., *et al.* (1976) Search for organic and volatile inorganic components in two surface samples from the Chryse Planitia region of Mars, *J. Geophys. Res.*, **82**, 4641-4658.
- Billebaud, F., Brillet, J., Lellouch, E., *et al.* (2009) Observations of CO in the atmosphere of Mars with PFS onboard Mars Express, *Planet. Space Sci.*, **57**, 1446-1457.
- Blamont, J. E., and Chassefière, E. (1993) First detection of ozone in the middle atmosphere of Mars from solar occultation measurements, *Icarus*, **104**, 324–336.
- Bogard, D. D., Clayton, R. N., Marti, K., *et al.* (2001) Martian volatiles : isotopic composition, origin, and evolution, *Space Sci. Rev.*, **96**, 425-58.
- Bougher, S. W., Roble, R. G., Ridley, E. C., *et al.* (1990) The Mars thermosphere 2. General circulation with coupled dynamics and composition, *J. Geophys. Res.*, **95**, 14811-14827.
- Carleton, N. P., and Traub, W. A. (1972) Detection of molecular oxygen on Mars, *Science*, **177**, 988-992.
- Chastain, B. K., and Chevrier, V. (2007) Methane clathrate hydrates as a potential source for martian atmospheric methane, *Planet. Space Sci.*, **55**, 1246–1256.
- Chassefière, E. (2009) Metastable methane clathrate particles as a source of methane to the martian atmosphere, *Icarus*, **204**, 137–144.

- Chaufray, J. Y., Bertaux, J. L., Leblanc, F., *et al.* (2008) Observation of the hydrogen corona with SPICAM on Mars Express, *Icarus*, **195**, 598-613.
- Chaufray, J. Y., Leblanc, F., Quémerais, E., *et al.* (2009) Martian oxygen density at the exobase deduced from O I 130.4-nm observations by Spectroscopy for the Investigation of the Characteristics of the Atmosphere of Mars on Mars Express, *J. Geophys. Res.*, **114**, E02006.
- Chung, C. Y., Chew, E. P., Cheng, B. M., *et al.* (2001) Temperature dependence of absorption cross-section of H₂O, HDO, and D₂O in the spectral region 140-193 nm, *Nucl. Instr. Meth. Phys. Res. A*, **467**, 1572-1576.
- Christensen, P. R., Bandfield, J. L., Bell, J. F., *et al.* (2003) Morphology and composition of the surface of Mars: Mars Odyssey THEMIS results, *Science*, **300**, 2056-2061.
- Clancy, R. T., and Nair, H. (1996) Annual (aphelion-perihelion) cycles in the photochemical behavior of the global Mars atmosphere, *J. Geophys. Res.*, **101**, 12785-12790.
- Clancy, R. T., Grossman, A. W., Wolff, M. J., *et al.* (1996) Water vapor saturation at low altitudes around Mars aphelion: A key to Mars Climate ?, *Icarus*, **122**, 36-62.
- Clancy, R. T., Wolff, M. J., and James, P. B. (1999) Minimal aerosol loading and global increases in atmospheric ozone during the 1996-1997 martian northern spring season, *Icarus*, **138**, 49-63.

- Clancy, R. T., Sandor, B. J., and Moriarty-Schieven, G. H. (2004) A measurement of the 362 GHz absorption line of Mars atmospheric H₂O₂, *Icarus*, **168**, 116-121.
- Clancy, R. T., Sandor, B. J., Wolff, M. J., *et al.* (2012) Extensive MRO CRISM observations of 1.27 μ m O₂ airglow in Mars polar night and their comparison to MRO MCS temperature profiles and LMD GCM simulations, *J. Geophys. Res.*, **117**, doi:10.1029/2011JE004018.
- Clancy, R. T., Sandor, B. J., García-Muñoz, A., *et al.* (2013a) First detection of Mars atmospheric hydroxyl: CRISM near-IR measurement versus LMD GCM simulation of OH Meinel band emission in the Mars polar winter stratosphere, *Icarus*, **226**, 272-281.
- Clancy, R. T., Sandor, B. J., Wolff, M. J., *et al.* (2013b) Correction to “Extensive MRO CRISM observations of 1.27 μ m O₂ airglow in Mars polar night and their comparison to MRO MCS temperature profiles and LMD GCM simulations”, *J. Geophys. Res.*, **118**, doi:10.1002/jgre.20073.
- Clancy, R. T., Wolff, M. J., Lefèvre, F., *et al.* (2014) MARCI global daily ozone mapping and comparison to LMD GCM simulations: polar dynamics, Hellas basin, and heterogeneous chemistry, paper presented at Fifth International Workshop on Mars Atmosphere: Modelling and Observations, Oxford.

- Clegg, S. M., and Abbatt, J. P. D. (2001) Uptake of gas-phase SO₂ and H₂O₂ by ice surfaces: Dependence on partial pressure, temperature, and surface activity, *J. Phys. Chem. A*, **105**, 6630-6636.
- Connes, P., Noxon, J. F., Traub, W. A., and Carleton, N. P. (1979) O₂(¹Δ) emission in the day and night airglow of Venus, *Astrophys. J.*, **233**, 29–32, doi:10.1086/183070.
- Cooper, P. L., and Abbatt, J. P. D. (1996) Heterogeneous interactions of OH and HO₂ radicals with surfaces characteristic of atmospheric particulate matter, *J. Phys. Chem.*, **100**, 2249–2254.
- Cox, C., Saglam, A., Gérard, J. C., *et al.* (2008) Distribution of the ultraviolet nitric oxide martian night airglow : observations from Mars Express and comparisons with a one-dimensional model, *J. Geophys. Res.*, **113**, doi :10.1029/2007JE003037.
- Crisp, D., Meadows, V. S., Bézard, B., *et al.* (1996) Ground-based near-infrared observations of the Venus nightside : 1.27 μm O₂(¹Δ_g) airglow from the upper atmosphere, *J. Geophys. Res.*, **101**, 4577-4593.
- Crowley, J. N., Ammann, M., Cox, R. A., *et al.* (2010) Evaluated kinetic and photochemical data for atmospheric chemistry: Volume V – heterogeneous reactions on solid substrates, *Atmos. Chem. Phys.*, **10**, 9059-9223.

- Encrenaz, T., Greathouse, T. K., Bézard, B., *et al.* (2002) A stringent upper limit of the H₂O₂ abundance in the martian atmosphere, *Astron. Astrophys.*, **396**, 1037-1044.
- Encrenaz, T., Bézard, B., Greathouse, T. K., *et al.* (2004) Hydrogen peroxide on Mars: Evidence for spatial and seasonal variations, *Icarus*, **170**, 424-429.
- Encrenaz, T., Fouchet, T., Melchiorri, R., *et al.* (2006) Seasonal variations of the martian CO over Hellas as observed by OMEGA/Mars Express, *Astron. Astrophys.*, **459**, 265-270.
- Encrenaz T., Greathouse, T. K., Richter, M. J., *et al.* (2008) Simultaneous mapping of H₂O and H₂O₂ on Mars from high-resolution imaging spectroscopy, *Icarus*, **195**, 547-555.
- Encrenaz, T., Greathouse, T. K., Richter, M. J., *et al.* (2011) A stringent upper limit to SO₂ in the martian atmosphere, *Astron. Astrophys.*, **530**, A37.
- Encrenaz, T., Greathouse, T. K., Lefèvre, F., and Atreya, S. K. (2012) Hydrogen peroxide on Mars: Observations, interpretation, and future plans, *Planet. Space. Sci.*, **68**, 3-17.
- Espenak, F., Mumma, M. J., Kostiuk, T., *et al.* (1991) Ground-based infrared measurements of the global distribution of ozone in the atmosphere of Mars, *Icarus*, **92**, 252–262.
- Fast, K., Kostiuk, T., Espenak, F., *et al.* (2006) Ozone abundance on Mars from infrared heterodyne spectra. I. Acquisition, retrieval, and anticorrelation with water vapor, *Icarus*, **181**, 419-431.

- Fast, K., Kostiuk, T., Lefèvre, F., *et al.* (2009) Comparison of HIPWAC and Mars Express SPICAM observations of ozone on Mars 2006-2008 and variation from 1993 IRHS observations, *Icarus*, **203**, 20-27.
- Fedorova, A., Korablev, O., Perrier, S., *et al.* (2006a) Observations of O₂ 1.27 μ m dayglow by SPICAM IR: Seasonal distribution for the first martian year of Mars Express, *J. Geophys. Res.*, **111**, doi:10.1029/2006JE002694.
- Fedorova, A., Korablev, O., Bertaux, J. L., *et al.* (2006b) Mars water vapor abundance from SPICAM IR spectrometer: Seasonal and geographic distributions, *J. Geophys. Res.*, **111**, doi:10.1029/2006JE002695.
- Fedorova A., Lefèvre, F., Guslyakova, S., *et al.* (2012) The O₂ nightglow in the martian atmosphere by SPICAM onboard of Mars-Express, *Icarus*, **219**, 596-608.
- Fonti, S., and Marzo, G. A. (2010) Mapping the methane on Mars, *Astron. Astrophys.* **512**, A51, 2010.
- Formisano, V., Atreya, S. K., Encrenaz, T., *et al.* (2004) Detection of methane in the atmosphere of Mars, *Science*, **306**, 1758-1761.
- Fouchet, T., Lellouch, E., Ignatiev, N. I., *et al.* (2007) Martian water vapor: Mars Express PFS/LW observations, *Icarus*, **190**, 32-49.

- García Muñoz, A., McConnell, J. C., McDade, I. C., *et al.* (2005) Airglow on Mars: Some model expectations for the OH Meinel bands and the O₂ IR atmospheric band, *Icarus*, **176**, 75-95.
- Geminale, A., Formisano, V., and Sindoni, G. (2011) Mapping methane in martian atmosphere with PFS-MEX data, *Planet. Space Sci.*, **59**, 137-148.
- Gérard, J.-C., Cox, C., Soret, L., *et al.* (2009) Concurrent observations of the ultraviolet nitric oxide and infrared O₂ nightglow emissions with Venus Express, *J. Geophys. Res.*, **114**, doi:10.1029/2009JE003371.
- Glavin, D. P., Freissinet, C., Miller, K. E., *et al.* (2013) Evidence for perchlorates and the origin of chlorinated hydrocarbons detected by SAM at the Rocknest aeolian deposit in Gale crater, *J. Geophys. Res.*, **118**, 1955-1973.
- Gough, R. V., Turley, J. J., Ferrell, G. R., *et al.* (2011) Can rapid loss and high variability of martian methane be explained by surface H₂O₂?, *Planet. Space Sci.*, **59**, 238-246.
- Haywood, J., and Boucher, O. (2000) Estimates of the direct and indirect radiative forcing due to tropospheric aerosols: a review, *Rev. Geophys.*, **38**, 513-543.
- Hartogh, P., Jarchow, C., Lellouch, E., *et al.* (2010a) Herschel/HIFI observations of HCl, H₂O₂, and O₂ in the martian atmosphere – initial results, *Astron. Astrophys.*, **521**, doi: 10.1051/0004-6361/201015160.

- Hartogh, P., Blecka, M. I., Jarchow, C., *et al.* (2010b) First results on martian carbon monoxide from Herschel/HIFI observations, *Astron. Astrophys.*, **521**, doi:10.1051/201015159.
- Hecht, M. H., Kounaves, S. P., Quinn, R. C., *et al.* (2009) Detection of Perchlorate and the Soluble Chemistry of martian Soil at the Phoenix Lander Site, *Science*, **325**, 64-67.
- Kaplan, L. D., Connes, J., and Connes, P. (1969) Carbon monoxide in the martian atmosphere, *Astrophys. J.*, **157**, 187-192.
- Keppler, F., Vigano, I., McLeod, A., *et al.* (2012) Ultraviolet-radiation-induced methane emissions from meteorites and the Martian atmosphere, *Nature*, **486**, 93-96.
- Kliore, A. J., Cain, D. L., Levy, G. S., *et al.* (1965) Occultation experiment: Result of the first direct measurement of Mars' atmosphere and ionosphere, *Science*, **149**, 1243-1245.
- Kliore, A. J., Fjeldbo, G., Seidel, B. L., *et al.* (1973) S band radio occultation measurements of the atmosphere and topography of Mars with Mariner 9: extended mission coverage of polar and intermediate latitudes, *J. Geophys. Res.*, **78**, 4331-4351.
- Knak Jensen, S. J., Skibsted, J., Jakobsen, H. J., *et al.* (2014) A sink for methane on Mars ? The answer is blowing in the wind, *Icarus*, **236**, 24-27.

- Kong, T. Y., and McElroy, M. B. (1977a) Photochemistry of the martian atmosphere, *Icarus*, **32**, 168–189.
- Kong, T. Y., and McElroy, M. B. (1977b) The global distribution of O₃ on Mars, *Planet. Space Sci.*, **25**, 839-857.
- Krasitski, O. P. (1978) A model for the diurnal variations of the composition of the martian atmosphere, *Cosmic Res.*, **16**, 434-442.
- Krasnopolsky, V. A., and Parshev, V. A. (1979) Ozone photochemistry of the martian lower atmosphere, *Planet. Space Sci.*, **27**, 113–120.
- Krasnopolsky, V. A. (1993) Photochemistry of the martian atmosphere (mean conditions), *Icarus*, **101**, 313–332.
- Krasnopolsky, V. A., Bowyer, S., Chakrabarti, S., *et al.* (1994) First measurement of helium on Mars: implications for the problem of radiogenic gases on the terrestrial planets, *Icarus*, **109**, 337-351.
- Krasnopolsky, V. A. (1995) Uniqueness of a solution of a steady state photochemical problem: Applications to Mars, *J. Geophys. Res.*, **100**, 3263-3276.
- Krasnopolsky, V. A. (1997) Photochemical mapping of Mars, *J. Geophys. Res.*, **102**, 13313-13320.

- Krasnopolsky, V. A., Bjoraker, G. L., Mumma, M. J., *et al.* (1997) High-resolution spectroscopy of Mars at 3.7 and 8 μm : A sensitive search for H_2O_2 , H_2CO , HCl , and CH_4 , and detection of HDO , *J. Geophys. Res.*, **102**, 6525-6534.
- Krasnopolsky, V. A., and Bjoraker, G.L. (2000) Mapping of Mars $\text{O}_2(^1\Delta)$ dayglow, *J. Geophys. Res.*, **105**, 20179-20188, 2000.
- Krasnopolsky, V. A., and Feldman, P. D. (2001) Detection of molecular hydrogen in the atmosphere of Mars, *Science*, **294**, 1914-1917.
- Krasnopolsky, V. A. (2003a) Spectroscopic mapping of Mars CO mixing ratio: detection of north-south asymmetry, *J. Geophys. Res.*, **108**, doi:10.1029/2002JE001926.
- Krasnopolsky, V. A. (2003b) Spectroscopy of Mars O_2 1.27 μm dayglow at four seasonal points, *Icarus*, **165**, 315-325.
- Krasnopolsky, V. A., Maillard, J. P., and Owen, T. C. (2004) Detection of methane in the martian atmosphere: evidence for life? *Icarus*, **172**, 537-547.
- Krasnopolsky, V. A., and Gladstone, G. R. (2005a) Helium on Mars and Venus: EUVE observations and modeling, *Icarus*, **176**, 395-407.

- Krasnopolsky, V. A. (2005b) A sensitive search for SO₂ in the martian atmosphere: Implications for seepage and origin of methane, *Icarus*, **178**, 487-492.
- Krasnopolsky, V.A. (2006a) Photochemistry of the martian atmosphere: Seasonal, latitudinal, and diurnal variations, *Icarus*, **185**, 153–170.
- Krasnopolsky, V. A. (2006b) A sensitive search for nitric oxide in the lower atmospheres of Venus and Mars: detection on Venus and upper limit for Mars, *Icarus*, **182**, 80-91.
- Krasnopolsky, V. A. (2006c) Some problems related to the origin of methane on Mars, *Icarus*, **180**, 359-367.
- Krasnopolsky, V. A. (2007) Long-term spectroscopic observations of Mars using IRTF/CSHELL: Mapping of O₂ dayglow, CO, and search for CH₄, *Icarus*, **190**, 93-102.
- Krasnopolsky, V. A. (2009) Seasonal variations of photochemical tracers at low and middle latitudes on Mars: Observations and models, *Icarus*, **201**, 564-569.
- Krasnopolsky, V. A. (2010) Solar activity variations of thermospheric temperatures on Mars and a problem of CO in the lower atmosphere, *Icarus*, **207**, 638-647.
- Krasnopolsky, V. A. (2011) Excitation of the oxygen nightglow on the terrestrial planets, *Planet. Space Sci.*, **59**, 754–766.

- Krasnopolsky, V. A. (2012) Search for methane and upper limits to ethane and SO₂ on Mars, *Icarus*, **217**, 144-152.
- Krasnopolsky, V. A. (2013) Night and day airglow of oxygen at 1.27 μ m on Mars, *Planet. Space Sci.*, **85**, 243-249, 2013.
- Kuiper, G. P. (1949) Survey of planetary atmospheres, in *The Atmospheres of the Earth and Planets* (Kuiper, G.P. Ed), Chicago Press, Chicago.
- Lane, A. L., Barth, C. A., Hord, C. W., *et al.* (1973) Mariner 9 ultraviolet spectrometer experiment: Observations of ozone on Mars, *Icarus*, **18**, 102– 108.
- Lebonnois, S., Quémerais, E., Montmessin, F., *et al.* (2006) Vertical distribution of ozone on Mars as measured by SPICAM/Mars Express using stellar occultations, *J. Geophys. Res.*, **111**, E09S05, doi :10.1029/2005JE002643.
- Lefèvre, F., Lebonnois, S., Montmessin, F., *et al.* (2004) Three-dimensional modeling of ozone on Mars, *J. Geophys. Res.*, **109**, E07004, doi:10.1029/2004JE002268.
- Lefèvre, F., Bertaux, J. L., Clancy, R. T. (2008) *et al.*, Heterogeneous chemistry in the atmosphere of Mars, *Nature*, **454**, 971-975.
- Lefèvre, F., and Forget, F. (2009) Observed variations of methane on Mars unexplained by known atmospheric chemistry and physics, *Nature*, **460**, 720-723.

- Lewis, J. S., and Carver, J. H. (1983) Temperature dependence of the carbon dioxide photoabsorption cross section between 1200 and 170 Angstroms, *J. Quant. Spectrosc. Radiat. Transfer*, **30**, 297–309.
- Lindner, B. L. (1988) Ozone on Mars: The effects of clouds and airborne dust, *Planet. Space Sci.*, **36**, 125–144.
- Liu, S. C., and Donahue, T. M. (1976) The regulation of hydrogen and oxygen escape from Mars, *Icarus*, **28**, 231-246.
- Maguire, W. C. (1977) Martian isotopic ratios and upper limits for possible minor constituents as derived from Mariner 9 infrared spectrometer data, *Icarus*, **32**, 85-97.
- Mahaffy, P. R., Webster, C. R., Atreya, S. K., *et al.*, Abundance and isotopic composition of gases in the martian atmosphere from the Curiosity rover, *Science*, **341**, 263-266.
- McElroy, M. B., and Donahue, T. M. (1972) Stability of the martian atmosphere, *Science*, **177**, 986–988.
- Maltagliati, L., Montmessin, F., Fedorova, A., *et al.* (2011) Evidence of water vapor in excess of saturation in the atmosphere of Mars, *Science*, **333**, 1868-1870.

- Maltagliati, L., Montmessin, F., Korablev, O., *et al.* (2013) Annual survey of water vapor vertical distribution and water-aerosol coupling in the martian atmosphere observed by SPICAM/Mex solar occultations, *Icarus*, **223**, 942-962.
- Melchiorri, R., Encrenaz, T., Fouchet, T., *et al.* (2007) Water vapor mapping on Mars using OMEGA/Mars Express, *Planet. Space Sci.*, **55**, 333-342.
- Montmessin, F., Forget, F., Rannou, P., *et al.* (2004) Origin and role of water ice clouds in the martian water cycle as inferred from a general circulation model, *J. Geophys. Res.*, **109**, E10004, doi:10.1029/2004JE002284.
- Montmessin, F., and Lefèvre, F. (2013) Transport-driven formation of a polar ozone layer on Mars, *Nature Geo.*, **6**, 930-933.
- Moudden, Y., and McConnell, J. C. (2007) Three-dimensional on-line modeling in a Mars general circulation model, *Icarus*, **188**, 18-34.
- Moudden, Y. (2007) Simulated seasonal variations of hydrogen peroxide in the atmosphere of Mars, *Planet. Space Sci.*, **55**, 2137-2143.
- Moreau, D., Esposito, L. W., and Brasseur, G. (1991) The chemical composition of the dust-free martian atmosphere: Preliminary results of a two-dimensional model, *J. Geophys. Res.*, **96**, 7933–7945.

- Mumma, M. J., Villanueva, G. L., Novak, R. E., *et al.* (2009) Strong release of methane on Mars in northern summer 2003, *Science*, **323**, 1041-1045.
- Nair, H., Allen, M., Anbar, A. D., *et al.* (1994) A photochemical model of the martian atmosphere, *Icarus*, **111**, 124– 150.
- Nier, A. O., Hanson, W. B., Seiff, A., *et al.* (1976) Composition of the martian atmosphere : Preliminary results from Viking 1, *Science*, **193**, 786-788, 1976.
- Nier, A. O., and McElroy, M. B. (1977) Composition and structure of Mars' upper atmosphere : Results from the neutral mass spectrometers on Viking 1 and 2, *J. Geophys. Res.*, **82**, 4341-4348.
- Novak, R., Mumma, M. J., DiSanti, M. D., *et al.* (2002) Mapping of ozone and water in the atmosphere of Mars near the 1997 aphelion, *Icarus*, **158**, 14-23.
- Noxon, J. F., Traub, W. A., Carleton, N. P., *et al.* (1976) Detection of O₂ dayglow emission from Mars and the martian ozone abundance, *Astrophys. J.*, **207**, 1025-1030, 1976.
- Owen, T., Biemann, K., Rushneck, D. R., *et al.* (1977) The composition of the atmosphere at the surface of Mars, *J. Geophys. Res.*, **82**, 4635-4639, 1977.
- Parkinson, T. D., and Hunten, D. M. (1972) Spectroscopy and aeronomy of O₂ on Mars, *J. Atmos. Sci.*, **29**, 1380–1390.

- Perrier, S., Bertaux, J. L., Lefèvre, F., *et al.* (2006) Global distribution of total ozone on Mars from SPICAM/MEX UV measurements, *J. Geophys. Res.*, **111**, E09S06, doi:10.1029/2006JE002681, 2006.
- Quinn, R. C., and Zent A. P. (1999) Peroxide-modified titanium dioxide: A chemical analog of putative martian soil oxidants, *Origins Life Evol. Biosphere*, **29**, 59-72.
- Sander, S. P., Abbatt, J. P. D., Barker, J. R., *et al.* (2011) *Chemical Kinetics and Photochemical Data for Use in Atmospheric Studies, Evaluation Number 17*, Jet Propulsion Laboratory, Pasadena.
- Shimazaki, T., and Shimizu, M. (1979) The seasonal variation of ozone density in the martian atmosphere, *J. Geophys. Res.*, **84**, 1269-1276.
- Shimazaki, T. (1981) A model of temporal variations in ozone density in the martian atmosphere, *Planet. Space Sci.*, **29**, 21-33.
- Sindoni, G., Formisano, V., and Geminale, A. (2011) Observations of water vapour and carbon monoxide in the martian atmosphere with the SWC of PFS/MEX, *Planet. Space Sci.*, **59**, 149-162.
- Smith, M. D. (2004) Interannual variability in TES atmospheric observations of Mars during 1999-2003, *Icarus*, **167**, 148-165.

- Smith, M. D., Wolff, M. J., Clancy, R. T., *et al.* (2009) Compact Reconnaissance imaging spectrometer observations of water vapor and carbon monoxide, *J. Geophys. Res.*, **114**, doi:10.1029/2008JE003288.
- Spinrad, H., Münch, G., and Kaplan, L. D. (1963) The detection of water vapor on Mars, *Astrophys. J.*, **137**, 1319-1321.
- Sprague, A. L., Boynton, W. V., Kerry, K. E., *et al.* (2004) Mars' south polar Ar enhancement: A tracer for south polar seasonal meridional mixing, *Science*, **306**, 1364-1367.
- Strickland, D.J., Thomas, G. E., and Sparks, P. R. (1972) Mariner 6 and 7 ultraviolet spectrometer experiment: Analysis of the O I 1304 and 1356 Å emissions, *J. Geophys. Res.*, **77**, 4052-4058.
- Summers, M. E., Lieb, B. J., Chapman, E., *et al.* (2002) Atmospheric biomarkers of subsurface life on Mars, *Geophys. Res. Lett.*, **29**, doi:10.1029/2002GL015377.
- Thompson, B. A., Harteck, P., and Reeves, R. R. (1963) Ultraviolet absorption coefficients of CO₂, CO, O₂, H₂O, N₂O, NH₃, NO, SO₂ and CH₄ between 1850 and 4000 Å, *J. Geophys. Res.*, **68**, 6431–6436.
- Trainer, M. G., Tolbert, M. A., McKay, C. P. *et al.* (2011) Limits on the trapping of atmospheric CH₄ in martian polar ice analogs, *Icarus*, **208**, 192-197.

- Traub, W. A., Carleton, N. P., Connes, P., *et al.* (1979) The latitude variation of O₂ dayglow and O₃ abundance on Mars, *Astrophys. J.*, **229**, 846–850.
- Trauger, J. T., and Lunine, J. I. (1983) Spectroscopy of molecular oxygen in the atmosphere of Venus and Mars, *Icarus*, **55**, 272-281.
- Tschimmel, M., Ignatiev, N. I., Titov, D. V., *et al.* (2008) Investigation of water vapor on Mars with PFS/SW of Mars Express, *Icarus*, **195**, 557-575.
- Villanueva, G. L., Mumma, M. J., Novak, R. E., *et al.* (2013) A sensitive search for organics (CH₄, CH₃OH, H₂CO, C₂H₆, C₂H₂, C₂H₄), hydroperoxyl, nitrogen compounds (N₂O, NH₃, HCN) and chlorine species on Mars using ground-based high-resolution infrared spectroscopy, *Icarus*, **223**, 11-27.
- Webster, C. R., Mahaffy, P. R., Atreya, S. K., *et al.* (2013) Low upper limit to methane abundance on Mars, *Science*, **342**, 355-357.
- Webster, C. R., Mahaffy, P. R., Atreya, S. K., *et al.* (2015) Mars methane detection and variability at Gale crater, *Science*, **347**, 415-427.
- Wong, A. S., Atreya, S. K., and Encrenaz, T. (2003) Chemical markers of possible hot spots on Mars, *J. Geophys. Res.*, **108**, E4, 5026, doi:10.1029/2002JE002003.

Yung, Y. L., Strobel, D. F., Kong, T. Y., *et al.* (1977) Photochemistry of nitrogen in the martian atmosphere, *Icarus*, **30**, 26-41.

Yung, Y. L., and DeMore W. B. (1999) *Photochemistry of Planetary Atmospheres*, Oxford Univ. Press, Oxford/New York.

Zahnle, K., Haberle, R. M., Catling, D. C., *et al.* (2008) Photochemical instability of the ancient martian atmosphere, *J. Geophys. Res.*, **113**, E11004, doi:10.1029/2008JE003160.

Zahnle, K., Freedman, R. S., and Catling, D. C. (2011) Is there methane on Mars?, *Icarus*, **212**, 493-50.

Species	Mixing ratio	Comments and references
CO ₂	0.955-0.960	Kuiper (1949); global and annually mean pressure 6.1 mbar (Kliore <i>et al.</i> 1973), Mahaffy <i>et al.</i> (2013)
N ₂	0.019-0.027	Owen <i>et al.</i> (1977), Mahaffy <i>et al.</i> (2013)
Ar	0.016-0.019	Owen <i>et al.</i> (1977), Mahaffy <i>et al.</i> (2013)
Ne	1-2.5 ppmv	Owen <i>et al.</i> (1977), Bogard <i>et al.</i> (2001)
Kr	0.3-0.36 ppmv	Owen <i>et al.</i> (1977), Bogard <i>et al.</i> (2001)
Xe	50-80 ppbv	Owen <i>et al.</i> (1977), Bogard <i>et al.</i> (2001)
H	(3-30)×10 ⁴ cm ⁻³	at 250 km for T_{∞} ≈300 & 200 K; Anderson and Hord (1971), Anderson (1974), Chaufray <i>et al.</i> (2008)
O	0.005-0.02	at 125 km; Strickland <i>et al.</i> (1972), Stewart <i>et al.</i> (1992), Chaufray <i>et al.</i> (2009)
O ₂	(1.2-1.4)×10 ⁻³	Barker (1972), Carleton and Traub (1972), Trauger and Lunine (1983), Hartogh <i>et al.</i> (2010a), Mahaffy <i>et al.</i> (2013)
CO	300-1600 ppmv	Kaplan <i>et al.</i> (1969), Krasnopolsky (2007), Billebaud <i>et al.</i> (2009), Smith <i>et al.</i> (2009), Hartogh <i>et al.</i> (2010b), Sindoni <i>et al.</i> (2011)
H ₂ O	0-70 pr. μm	Spinrad <i>et al.</i> (1963), Smith (2004), Fedorova <i>et al.</i> (2006b), Fouchet <i>et al.</i> (2007), Melchiorri <i>et al.</i> (2007), Tschimmel <i>et al.</i> (2008) Smith <i>et al.</i> (2009), Sindoni <i>et al.</i> (2011)
O ₃	0-60 μm-atm	Barth and Hord (1971), Barth <i>et al.</i> (1973), Clancy <i>et al.</i> (1999), Fast <i>et al.</i> (2006), Perrier <i>et al.</i> (2006), Lebonnois <i>et al.</i> (2006)
O ₂ (¹ Δ _g)	0.6-35 μm-atm *	Noxon <i>et al.</i> (1976), Fedorova <i>et al.</i> (2006a), Krasnopolsky (2013)
He	10 ppmv	Krasnopolsky <i>et al.</i> (1994), Krasnopolsky and Gladstone (2005a)
H ₂	17 ppmv	Krasnopolsky and Feldman (2001)
H ₂ O ₂	0-40 ppbv	Clancy <i>et al.</i> (2004), Encrenaz <i>et al.</i> (2004, 2012)
CH ₄	0-40 ppbv	Krasnopolsky <i>et al.</i> (2004), Formisano <i>et al.</i> (2004), Mumma <i>et al.</i> (2009), Geminale <i>et al.</i> (2011), Krasnopolsky (2012)
	0.7 -7 ppbv	Webster <i>et al.</i> (2015)
C ₂ H ₆	<0.2 ppbv	Krasnopolsky (2012), Villanueva <i>et al.</i> (2013)
H ₂ CO	<3 ppbv	Krasnopolsky <i>et al.</i> (1997), Villanueva <i>et al.</i> (2013)
CH ₃ OH	<6.9 ppbv	Villanueva <i>et al.</i> (2013)
H ₂ S	<100 ppbv	Maguire (1977)
HCl	<0.2 ppbv	Hartogh <i>et al.</i> (2010a)
SO ₂	<0.3 ppbv	Encrenaz <i>et al.</i> (2011), Krasnopolsky (2012)
NO	<1.7 ppbv	Krasnopolsky (2006b)
HCN	<2.1 ppbv	Villanueva <i>et al.</i> (2013)

First detections along with the latest data are given.

* O₂(¹Δ_g) dayglow at 1.27 μm is measured in MegaRayleigh; 1 MR = 1.67 μm-atm of O₂(¹Δ_g) for this airglow.

Table 13.1. Observed chemical composition of the martian atmosphere.

Reaction	Rate coefficient	Column rate
$\text{CO}_2 + h\nu \rightarrow \text{CO} + \text{O}$	—	1.49+12
$\text{CO}_2 + h\nu \rightarrow \text{CO} + \text{O}(^1\text{D})$	—	2.36+10
$\text{O}_2 + h\nu \rightarrow \text{O} + \text{O}$	—	1.70+11
$\text{O}_2 + h\nu \rightarrow \text{O} + \text{O}(^1\text{D})$	—	1.11+10
$\text{H}_2\text{O} + h\nu \rightarrow \text{H} + \text{OH}$	—	1.76+10
$\text{HO}_2 + h\nu \rightarrow \text{OH} + \text{O}$	2.6×10^{-4}	4.23+10
$\text{H}_2\text{O}_2 + h\nu \rightarrow \text{OH} + \text{OH}$	4.2×10^{-5}	5.68+10
$\text{O}_3 + h\nu \rightarrow \text{O}_2(^1\Delta) + \text{O}(^1\text{D})$	3.4×10^{-3}	6.38+12
$\text{O}(^1\text{D}) + \text{CO}_2 \rightarrow \text{O} + \text{CO}_2$	$7.4 \times 10^{-11} e^{120/T}$	6.42+12
$\text{O}(^1\text{D}) + \text{H}_2\text{O} \rightarrow \text{OH} + \text{OH}$	2.2×10^{-10}	1.50+9
$\text{O}(^1\text{D}) + \text{H}_2 \rightarrow \text{OH} + \text{H}$	1.1×10^{-10}	1.04+8
$\text{O}_2(^1\Delta) + \text{CO}_2 \rightarrow \text{O}_2 + \text{CO}_2$	10^{-20}	4.94+12
$\text{O}_2(^1\Delta) \rightarrow \text{O}_2 + h\nu$	2.24×10^{-4}	1.46+12
$\text{O} + \text{CO} + \text{CO}_2 \rightarrow \text{CO}_2 + \text{CO}_2$	$2.2 \times 10^{-33} e^{-1780/T}$	5.15+7
$\text{O} + \text{O} + \text{CO}_2 \rightarrow \text{O}_2 + \text{CO}_2$	$1.2 \times 10^{-32} (300/T)^2$	2.55+10
$\text{O} + \text{O}_2 + \text{CO}_2 \rightarrow \text{O}_3 + \text{CO}_2$	$1.4 \times 10^{-33} (300/T)^{2.4}$	6.45+12
$\text{H} + \text{O}_2 + \text{CO}_2 \rightarrow \text{HO}_2 + \text{CO}_2$	$1.7 \times 10^{-31} (300/T)^{1.6}$	1.93+12
$\text{O} + \text{HO}_2 \rightarrow \text{OH} + \text{O}_2$	$3 \times 10^{-11} e^{200/T}$	1.64+12
$\text{O} + \text{OH} \rightarrow \text{O}_2 + \text{H}$	$2.2 \times 10^{-11} e^{120/T}$	3.64+11
$\text{CO} + \text{OH} \rightarrow \text{CO}_2 + \text{H}$	1.5×10^{-13}	1.64+12
$\text{H} + \text{O}_3 \rightarrow \text{OH} + \text{O}_2$	$1.4 \times 10^{-10} e^{-470/T}$	6.17+10
$\text{H} + \text{HO}_2 \rightarrow \text{OH} + \text{OH}$	7.3×10^{-11}	2.36+10
$\text{H} + \text{HO}_2 \rightarrow \text{H}_2 + \text{O}_2$	$1.3 \times 10^{-11} (T/300)^{0.5} e^{-230/T}$	7.91+8
$\text{H} + \text{HO}_2 \rightarrow \text{H}_2\text{O} + \text{O}$	1.6×10^{-12}	5.18+8
$\text{OH} + \text{HO}_2 \rightarrow \text{H}_2\text{O} + \text{O}_2$	$4.8 \times 10^{-11} e^{250/T}$	1.71+10
$\text{HO}_2 + \text{HO}_2 \rightarrow \text{H}_2\text{O}_2 + \text{O}_2$	$2.3 \times 10^{-13} e^{600/T}$	5.75+10
$\text{OH} + \text{H}_2\text{O}_2 \rightarrow \text{HO}_2 + \text{H}_2\text{O}$	$2.9 \times 10^{-12} e^{-160/T}$	7.08+8
$\text{OH} + \text{H}_2 \rightarrow \text{H}_2\text{O} + \text{H}$	$3.3 \times 10^{-13} (T/300)^{2.7} e^{-1150/T}$	4.69+8
$\text{O} + \text{O}_3 \rightarrow \text{O}_2 + \text{O}_2$	$8 \times 10^{-12} e^{-2060/T}$	4.83+7
$\text{OH} + \text{O}_3 \rightarrow \text{HO}_2 + \text{O}_2$	$1.5 \times 10^{-12} e^{-880/T}$	1.30+7
$\text{HO}_2 + \text{O}_3 \rightarrow \text{OH} + \text{O}_2 + \text{O}_2$	$10^{-14} e^{-490/T}$	1.77+8
$\text{H}_2\text{O}_2 + \text{O} \rightarrow \text{OH} + \text{HO}_2$	$1.4 \times 10^{-12} e^{-2000/T}$	6.76+6
$\text{NO}_2 + h\nu \rightarrow \text{NO} + \text{O}$	0.0037	7.26+10
$\text{NO}_2 + \text{O} \rightarrow \text{NO} + \text{O}_2$	$5.6 \times 10^{-12} e^{180/T}$	1.78+10
$\text{NO} + \text{HO}_2 \rightarrow \text{NO}_2 + \text{OH}$	$3.5 \times 10^{-12} e^{250/T}$	9.04+10
diffusion-limited flux of H_2	$V_{\text{H}_2} = 1.14 \times 10^{13} / [\text{M}]_{79\text{km}}$	2.18+8
loss of H_2O_2 at the surface	$V_{\text{H}_2\text{O}_2} = 0.02$	3.43+7
loss of O_3 at the surface	$V_{\text{O}_3} = 0.02$	6.13+7
photolysis of O_2 above 80 km ^a	$V_{\text{O}_2} = 0.32$	1.20+10

Photolysis frequencies are in s^{-1} , second and third order reaction rate coefficients are in $\text{cm}^3 \text{s}^{-1}$ and $\text{cm}^6 \text{s}^{-1}$, respectively. Velocities V are in cm s^{-1} . Photolysis frequencies for HO_2 , H_2O_2 , O_3 , and NO_2 refer to the lower atmosphere and are calculated for $\lambda > 200 \text{ nm}$ at 1.517 AU. Column reaction rates are in $\text{cm}^{-2} \text{s}^{-1}$. They are multiplied by $(1 + z/R)^2$ at each altitude z to account for Mars sphericity (R being the Mars radius) and integrated from 1 to 79 km. 1.49×10^{12} is noted 1.49+12.

Table 13.2. Main reactions in the lower and middle atmosphere of Mars, their rate coefficients, and column rates in the globally-averaged model of Krasnopolsky (2010). The photolysis frequencies and column rates are dayside-mean. Velocity of H_2 at the upper boundary is that of

the diffusion-limited flux. As suggested by Zahnle et al. (2008), a surface sink of O_3 and H_2O_2 is assumed to balance the escape of hydrogen to space and maintain the atmosphere's redox budget. It is possible to check the balance for each species in the model by comparing its column production and loss rates in the table. For example, H_2 is formed by $H + HO_2$ with a rate of $7.91 \times 10^8 \text{ cm}^{-2} \text{ s}^{-1}$ and lost in the reactions with $O(^1D)$ and OH , with rates of 1.04×10^8 and $4.69 \times 10^8 \text{ cm}^{-2} \text{ s}^{-1}$ respectively. The difference between the production and loss, $2.18 \times 10^8 \text{ cm}^{-2} \text{ s}^{-1}$, escapes to the space (V_{H_2}). The escape of H_2 is balanced by the surface loss of oxygen in H_2O_2 and O_3 , so that $3.43 \times 10^7 + 3 \times 6.13 \times 10^7 = 2.18 \times 10^8 \text{ cm}^{-2} \text{ s}^{-1}$. Balance of all other species may be checked in the same way.

FIGURES LEGENDS

Figure 13.1. Seasonal evolution of the water vapor column (precipitable- μm) measured by the Thermal Infrared Spectrometer (TES) on board Mars Global Surveyor (Smith, 2004). Data are averaged over years 1999-2004. Contour intervals are 5, 10, 15, 20, 30, 40, 50, and 60 precipitable- μm .

Figure 13.2. Zonally-averaged distribution of water vapor calculated by the LMD global climate model at aphelion ($L_s = 70^\circ$, left) and perihelion ($L_s = 250^\circ$, right). The simulation was performed with an updated version of the model described by Montmessin *et al.* (2004).

Figure 13.3. Zonally-averaged distribution of odd hydrogen species calculated by the LMD global climate model for daytime conditions at aphelion ($L_s = 70^\circ$, top row) and perihelion ($L_s = 250^\circ$, bottom row). Left: atomic hydrogen H (ppbv). Strong production of H by reactions (7-9) and weak loss by reactions (18-19) leads to a maximum at high altitudes. Note the two order of magnitude increase from aphelion to perihelion. At both periods, downward transport also brings H-enriched air towards lower altitudes above the winter pole; center: hydroxyl radical OH (pptv). OH peaks at the top at the hygropause at mid-to-low latitudes. Maxima at high latitudes are due to large quantities of H and subsequent reaction (28); right: hydroperoxy radical HO_2 (ppbv). From the model of Lefèvre *et al.* (2004) after two martian years of simulation. Long-lived species O_2 , CO, H_2 are chemically integrated but were initialized to their observed mean mixing ratio (1400 ppmv, 800 ppmv, 15 ppmv, respectively) at the beginning of the model run.

Figure 13.4. Left: CO production and loss rates calculated at local noon and $L_s = 0^\circ$, for a latitude of 30° . Right: Zonally-averaged distribution of carbon monoxide CO (ppmv) calculated by the LMD global climate model for daytime conditions at northern spring equinox ($L_s = 0^\circ$). At high altitudes, strong CO_2 photolysis and weak loss by reaction with OH lead to a large increase in CO. At this season, downward transport brings CO-enriched air towards lower altitudes above both poles. From the model of Lefèvre *et al.* (2004) after a uniform initialization of $\text{CO} = 800$ ppmv as measured by CRISM at low-to-mid latitudes and $L_s = 0^\circ$ (Smith *et al.*, 2009), followed by two martian years of simulation

Figure 13.5. Seasonal evolution of the CO mixing ratio (ppmv) as observed between September 2006-January 2009 by the CRISM instrument on the MRO spacecraft. The artifact caused by extreme dust loading between $L_s = 270^\circ$ - 305° (white square) is masked out. From Smith *et al.* (2009).

Figure 13.6. Zonally-averaged distribution of hydrogen peroxide H_2O_2 (ppbv) calculated by the LMD global climate model for daytime conditions at aphelion ($L_s = 70^\circ$, left) and perihelion ($L_s = 250^\circ$, right). The distribution of H_2O_2 is tightly correlated to that of its source HO_2 . From the model of Lefèvre *et al.* (2004).

Figure 13.7. Observations of H_2O_2 on Mars. Left: First mapping of the H_2O_2 mixing ratio (units of 10^{-8}) obtained in June 2003 at $L_s = 206^\circ$ (Encrenaz *et al.*, 2004). Spatial variations are thought to be related to variations in H_2O amount. Right: the seasonal cycle of H_2O_2 on Mars. Observations in the infrared (TEXES) and models refer to 20°N for $L_s = 0-180^\circ$ and to 20°S for $L_s = 180-360^\circ$, in order to match as best as possible the observing conditions induced by the axial tilt of the planet. Submillimeter observations by Clancy *et al.* (2004, JCMT) refer to the entire disk. The points determined from Herschel at $L_s = 77^\circ$ (HERSCHEL/HIFI 2010) and TEXES 2001 at $L_s = 112^\circ$ are upper limits. GCM simulations updated from Lefèvre *et al.* (2008) ignore (yellow curve) or include (blue curve) heterogeneous chemistry. Error bars for the GCM represent variability (2σ). Model values by Krasnopolsky (2009) and Moudden (2007) are indicated by blue and green circles, respectively. Updated from Encrenaz *et al.* (2012).

Figure 13.8. Zonally-averaged distribution of atomic oxygen O (left column, in ppmv) and ozone O_3 (right column, in ppbv) calculated by the LMD global climate model for daytime conditions. Top: near aphelion ($L_s = 70^\circ$). Bottom: near perihelion ($L_s = 250^\circ$). From the model of Lefèvre *et al.* (2004) after two martian years of simulation. Long-lived species O_2 , CO, H_2 are chemically integrated but were initialized to their observed mean value (1.4×10^{-3} , 800 ppmv, 15 ppmv, respectively) at the beginning of the model run.

Figure 13.9. Mean photochemical lifetime of the O_x family ($\text{O} + \text{O}(^1\text{D}) + \text{O}_3$) calculated by the model of Lefèvre *et al.* (2004) at 40°N and local noon for $L_s = 70^\circ$ (solid curve) and $L_s = 250^\circ$ (dashed curve). Rise of the hygropause and the increase in upper atmosphere H_2O from aphelion to perihelion cause a dramatic reduction of the O_x lifetime above 20 km.

Figure 13.10. Seasonal evolution of the daytime ozone column ($\mu\text{m-atm}$). Left: ultraviolet measurements from the SPICAM instrument on Mars-Express averaged over martian years 27-30 (updated from Perrier *et al.*, 2006). Right: Three-dimensional simulation by the LMD global climate model with photochemistry described by Lefèvre *et al.* (2004), with updated kinetics and improved water cycle.

Figure 13.11. Nighttime O_3 vertical profile (molecule cm^{-3}) observed from 2004 to 2011 by the SPICAM instrument on Mars-Express between 70°S and 80°S and covering $L_s = 40^\circ\text{-}100^\circ$. In the southern hemisphere polar night, a secondary maximum peaking at 50 km is detected above the near-surface O_3 layer that is typical of polar regions in winter. Dust opacity prevents the observation below ~ 20 km. From Montmessin and Lefèvre (2013).

Figure 13.12. Ozone column ($\mu\text{m-atm}$) measured from Earth by infrared heterodyne spectroscopy (black symbols, Fast *et al.*, 2006) and from the Hubble Space Telescope Faint Object Spectrograph in the ultraviolet (open symbols, Clancy *et al.*, 1999). Left: Mars 1995, $L_s = 74^\circ$. Right: June 1988, $L_s = 208^\circ$.

Figure 13.13. Examples of O_3 nighttime vertical profiles (molecules cm^{-3}) measured at low latitudes. The data were obtained by stellar occultation with the SPICAM instrument on board Mars-Express. Left: near aphelion at $L_s = 60^\circ$ (29°S , 17°E). Right: in northern summer at $L_s = 132^\circ$ (16°N , 328°E). In both cases dust opacity prevents the observation below ~ 25 km. From Lebonnois *et al.* (2006).

Figure 13.14. Seasonal evolution of the vertically-integrated $\text{O}_2(^1\Delta_g)$ dayglow at $1.27 \mu\text{m}$, in units of Mega-Rayleigh ($1 \text{ MR} = 10^{12} \text{ photons cm}^{-2} \text{ s}^{-1} (4\pi \text{ ster})^{-1} = 4.5 \times 10^{15} \text{ cm}^{-2} = 1.7 \mu\text{m-atm}$ for the dayglow at $1.27 \mu\text{m}$). Left: Satellite observations averaged over 2004-2012 with the infrared channel of SPICAM on Mars Express (updated from Fedorova *et al.*, 2006a). Right: Three-dimensional simulation by the LMD global climate model with photochemistry described by Lefèvre *et al.* (2004), with updated kinetics and improved water cycle. Calculations were made with a $\text{O}_2(^1\Delta_g)$ quenching rate by CO_2 equal to $0.5 \times 10^{-20} \text{ cm}^3 \text{ s}^{-1}$.

Figure 13.15. The $\text{O}_2(^1\Delta_g)$ nightglow observed over both polar regions by CRISM on Mars Reconnaissance Orbiter. Left: Averaged $\text{O}_2(^1\Delta_g)$ volume emission profiles (kR km^{-1}) over $L_s = 74^\circ\text{-}96^\circ$ for latitude bins of $70^\circ\text{S-}80^\circ\text{S}$ (dashed lines) and $80^\circ\text{S-}90^\circ\text{S}$ (solid lines). Right: Averaged $\text{O}_2(^1\Delta_g)$ volume emission profiles (kR km^{-1}) over $L_s = 266^\circ\text{-}301^\circ$ for latitude bins of $70^\circ\text{N-}80^\circ\text{N}$ (dashed lines) and $80^\circ\text{N-}90^\circ\text{N}$ (solid lines). From Clancy *et al.* (2013b).

Figure 13.16. A schematic of the vertical and latitudinal distribution of the $O_2(^1\Delta_g)$ emission (zonally-averaged, in $kR\ km^{-1}$) as simulated by the LMD general circulation model for $L_s = 95^\circ$ - 100° . Two primary pathways exist for the production of $O_2(^1\Delta_g)$: 1) Over solar illuminated latitudes, the photolysis of ozone leads at this season to $O_2(^1\Delta_g)$ emission in a layer located above the hygropause between 25-40 km. A strong $O_2(^1\Delta_g)$ emission also outweighs the quenching by CO_2 near the surface in the southern hemisphere. This results from the dry surface conditions (see Figure 13.1) and subsequent large ozone densities at this season. 2) In the polar night, the three-body association of atomic oxygen transported downwards over the winter pole leads to $O_2(^1\Delta_g)$ emission between 45-60 km. The meridional stream function ($10^9\ kg\ s^{-1}$) is superimposed in white contour lines. They visualize the downwelling branch of the winter hemisphere Hadley circulation, bringing large amounts of O atoms produced in the upper atmosphere towards lower altitudes into the polar night. From Clancy *et al.* (2012).

Figure 13.17. Latitude-altitude distribution of the mixing ratio (zonal mean) of the main nitrogen species N, NO, and NO_2 at $L_s = 90^\circ$, calculated by the general circulation model of Moudden and McConnell (2007).

Figure 13.18. Vertical distribution of sulfur species ($molecule\ cm^{-3}$) for mean conditions below 80 km, assuming $SO_2 = 0.1\ ppbv$ at the surface. These results are obtained by inclusion of the SO_x chemistry in the 1D model of Krasnopolsky (2010). This chemistry involves updated data on photolysis of SO_2 and H_2SO_4 , reaction between SO_3 and H_2O , and heterogeneous reaction between SO_2 and H_2O_2 on ice particles. Uptake of H_2SO_4 on water-ice aerosols also occurs between 20-45 km and at night below 3 km. This explains the broad gas-phase H_2SO_4 peak between 3-20 km where uptake does not occur

Figure 13.19. Methane mixing ratio (ppbv) observed from Earth by Mumma *et al.* (2009). Left: regions where methane appeared enhanced during summer 2003 ($L_s = 121^\circ$ - 155°). Right: latitudinal and temporal variability of methane. Profile a was obtained in February 2006 at $L_s = 17.2^\circ$. Profiles b, c, d were obtained in January-March 2003 between $L_s = 121^\circ$ - 155° .

Figure 13.20. Methane mixing ratio (ppbv) measured by TLS on the rover Curiosity vs. martian sol. Sol 1 was on August 6th, 2012. All measurements were made at night, except the two marked “D” ingested during the day. The values with smaller error bars labeled EN were retrieved from the “methane enrichment” runs. From Webster *et al.* (2015).

Figure 13.21. Density profiles (molecule cm^{-3}) calculated by the global-mean photochemical model of Krasnopolsky (2010), using the chemical reaction rates listed in Table 2. O_2^* is $\text{O}_2(^1\Delta_g)$. The surface pressure is set to 6.1 hPa and the H_2O vertical column is 9.5 precipitable microns. The H_2O density profile is restricted by the saturation value. A downward flow of O and CO from the dissociation of O_2 and CO_2 above 80 km is also imposed at the upper boundary. The calculated abundances of the major photochemical products are 1600 ppmv for O_2 , 120 ppmv for CO, 20 ppmv for H_2 , 0.9 $\mu\text{m-atm}$ for O_3 , 1.5 MR or 2.5 $\mu\text{m-atm}$ for $\text{O}_2(^1\Delta_g)$, and 7.6 ppbv for H_2O_2 . These values are in reasonable agreement with the observations, with the exception of CO that is underestimated by a factor of eight.

Figure 13.22. Ozone column ($\mu\text{m-atm}$) calculated by the 1D model of Krasnopolsky (2009) at different latitudes and seasons. The model includes an irreversible uptake coefficient of 3×10^{-4} for H_2O_2 on ice. This map can be compared to the SPICAM and ground-based observations of ozone displayed in Figures 13.10 and 13.12, respectively.

Figure 13.23. Modeled diurnal variations of the O_3 column ($\mu\text{m-atm}$), H_2O_2 (ppbv), the $\text{O}_2(^1\Delta_g)$ dayglow at $1.27 \mu\text{m}$ (solid line, in MR), and the $\text{O}_2(^1\Delta_g)$ airglow at $1.27 \mu\text{m}$ from the termolecular association of O atoms (dotted line, in kR). Top: results at $L_s = 112^\circ$. Bottom: results at $L_s = 173^\circ$. From Krasnopolsky (2006a).

Figure 13.24. Ozone column ($\mu\text{m-atm}$) calculated by the LMD general circulation model. Left: synoptic distribution in northern spring ($L_s = 30^\circ$) with a photochemical scheme taking into account heterogeneous reactions of HO_x on water-ice clouds. The observer is facing the 180° meridian at local noon, and the black contours correspond to Mars topography. Right: Comparison of the same GCM simulation with the ozone columns measured in the 50°N - 70°N latitude band by SPICAM (Perrier *et al.*, 2006), HST (Clancy *et al.*, 1999), and IRTF (Fast *et al.*, 2006). From Lefèvre *et al.* (2008).

Figure 13.25. Column-averaged mixing ratio of H_2O_2 calculated by the GM3 general circulation model (Moudden, 2007). Left : $L_s = 90^\circ$. Right : $L_s = 270^\circ$. The seasonal evolution of H_2O_2 calculated by this model is compared to observations in the right panel of Figure 13.7.

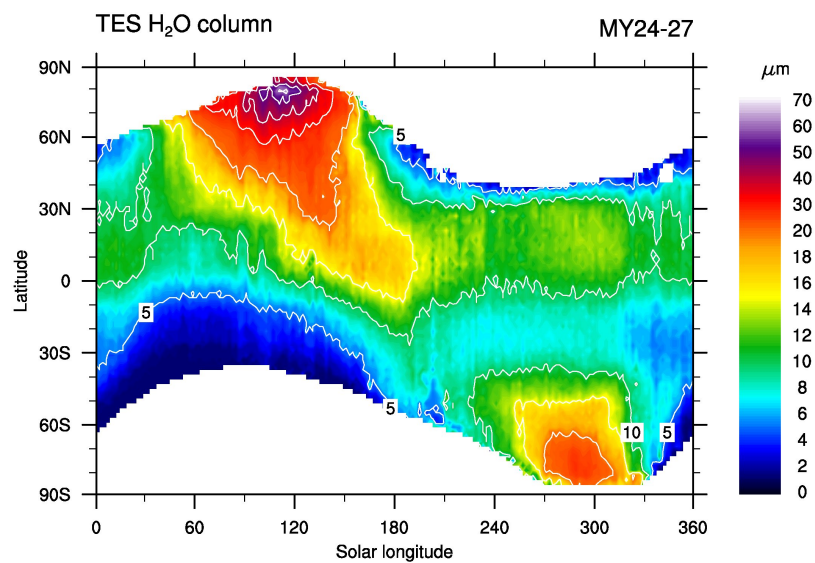


Figure 13.1. Seasonal evolution of the water vapor column (precipitable- μm) measured by the Thermal Infrared Spectrometer (TES) on board Mars Global Surveyor (Smith, 2004). Data are averaged over years 1999-2004. Contour intervals are 5, 10, 15, 20, 30, 40, 50, and 60 precipitable- μm .

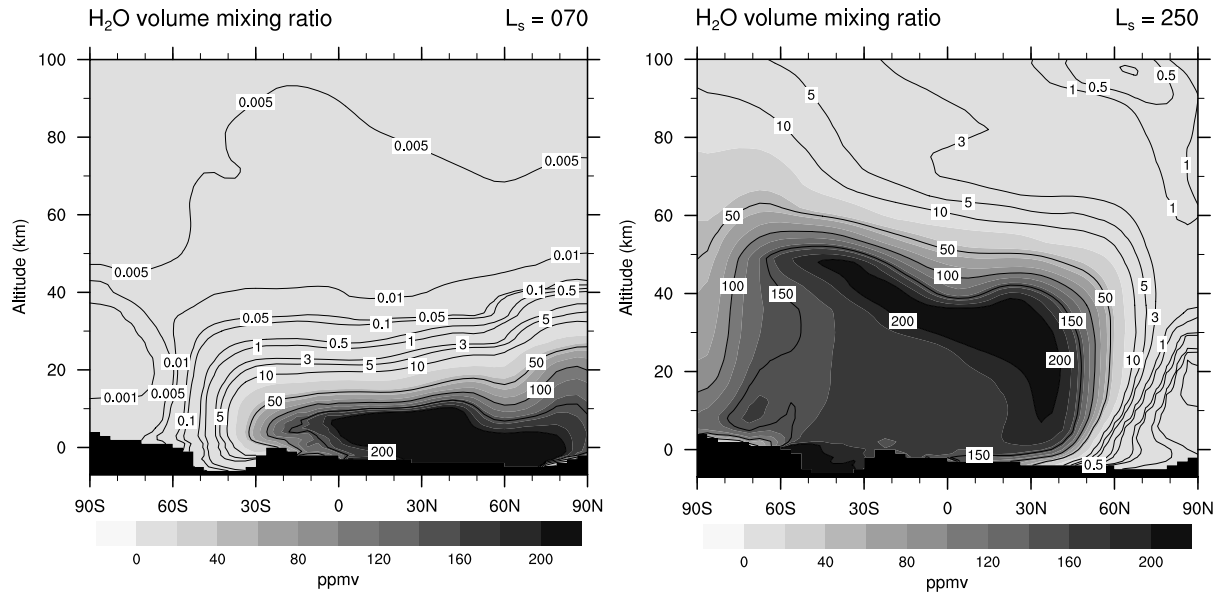


Figure 13.2. Zonally-averaged distribution of water vapor calculated by the LMD global climate model at aphelion ($L_s = 70^\circ$, left) and perihelion ($L_s = 250^\circ$, right). The simulation was performed with an updated version of the model described by Montmessin *et al.* (2004).

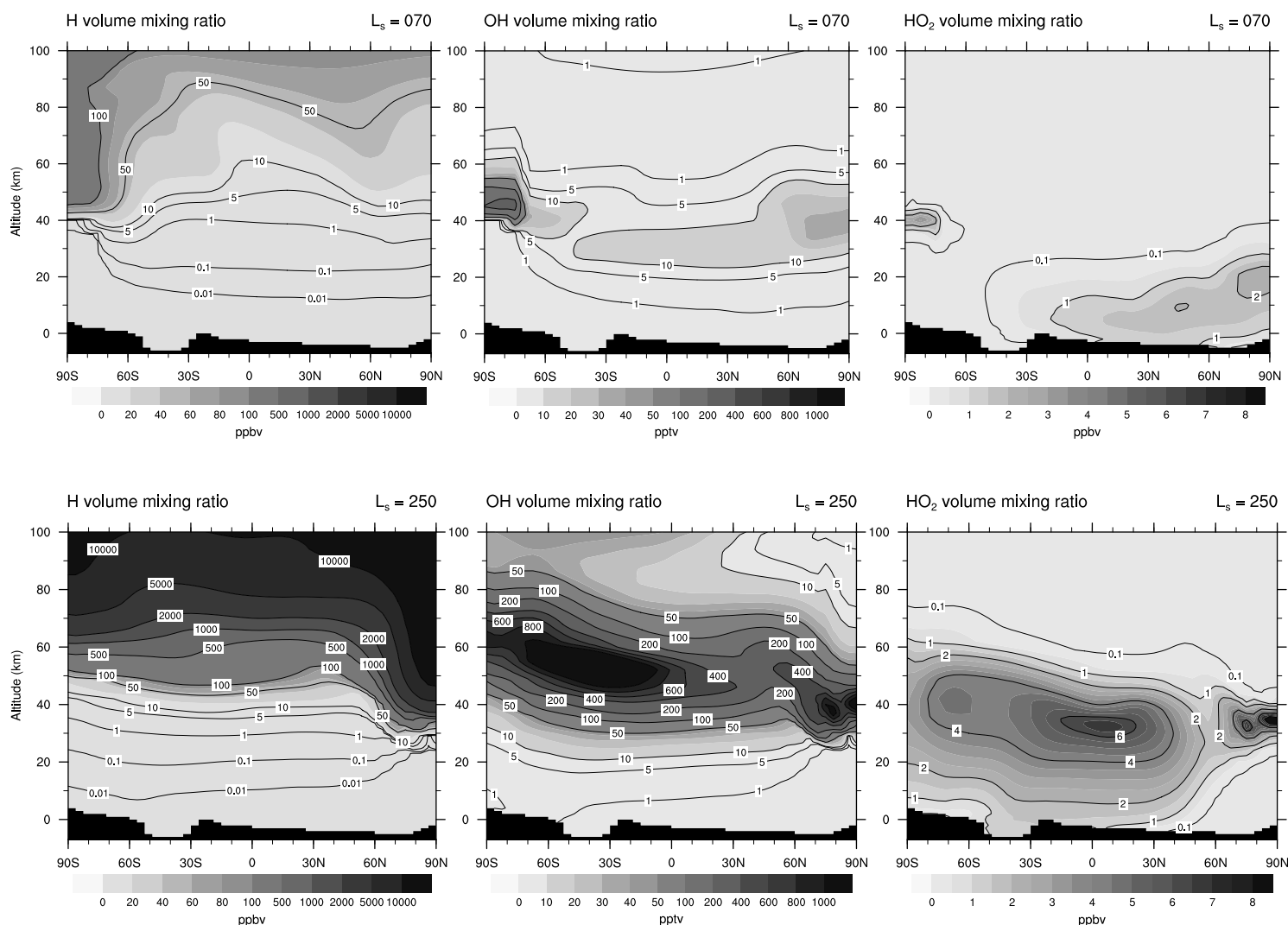


Figure 13.3. Zonally-averaged distribution of odd hydrogen species calculated by the LMD global climate model for daytime conditions at aphelion ($L_s = 70^\circ$, top row) and perihelion ($L_s = 250^\circ$, bottom row). Left: atomic hydrogen H (ppbv). Strong production of H by reactions (7-9) and weak loss by reactions (18-19) leads to a maximum at high altitudes. Note the two order of magnitude increase from aphelion to perihelion. At both periods, downward transport also brings H-enriched air towards lower altitudes above the winter pole; center: hydroxyl radical OH (pptv). OH peaks at the top at the hygropause at mid-to-low latitudes. Maxima at high latitudes are due to large quantities of H and subsequent reaction (28); right: hydroperoxy radical HO_2 (ppbv). From the model of Lefèvre *et al.* (2004) after two martian years of simulation. Long-

lived species O_2 , CO , H_2 are chemically integrated but were initialized to their observed mean mixing ratio (1400 ppmv, 800 ppmv, 15 ppmv, respectively) at the beginning of the model run.

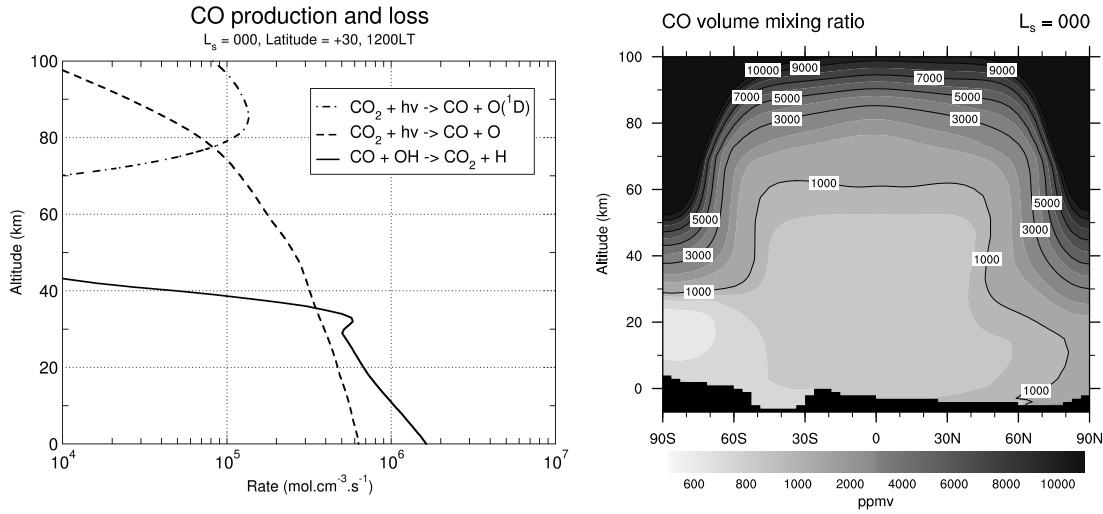


Figure 13.4. Left: CO production and loss rates calculated at local noon and $L_s = 0^\circ$, for a latitude of 30° . Right: Zonally-averaged distribution of carbon monoxide CO (ppmv) calculated by the LMD global climate model for daytime conditions at northern spring equinox ($L_s = 0^\circ$). At high altitudes, strong CO_2 photolysis and weak loss by reaction with OH lead to a large increase in CO. At this season, downward transport brings CO-enriched air towards lower altitudes above both poles. From the model of Lefèvre *et al.* (2004) after a uniform initialization of $\text{CO} = 800$ ppmv as measured by CRISM at low-to-mid latitudes and $L_s = 0^\circ$ (Smith et al., 2009), followed by two martian years of simulation.

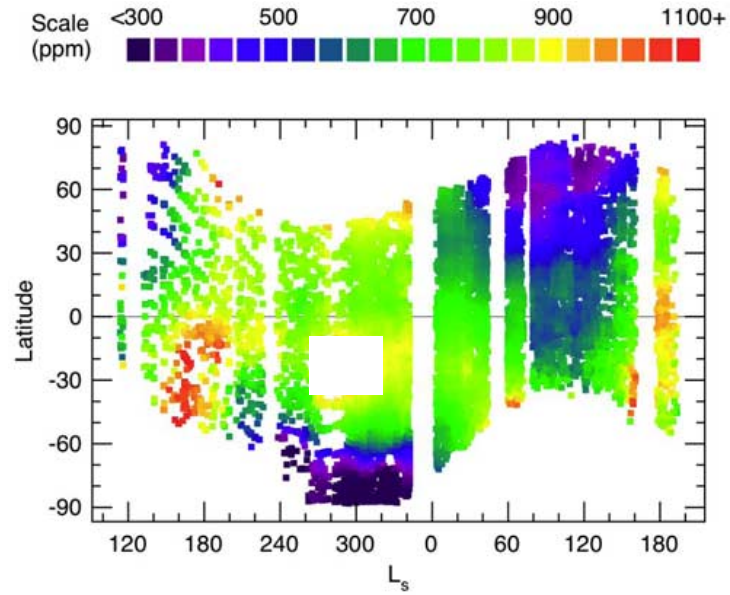


Figure 13.5. Seasonal evolution of the CO mixing ratio (ppmv) as observed between September 2006-January 2009 by the CRISM instrument on the MRO spacecraft. The artifact caused by extreme dust loading between $L_s = 270^\circ$ - 305° (white square) is masked out. From Smith *et al.* (2009).

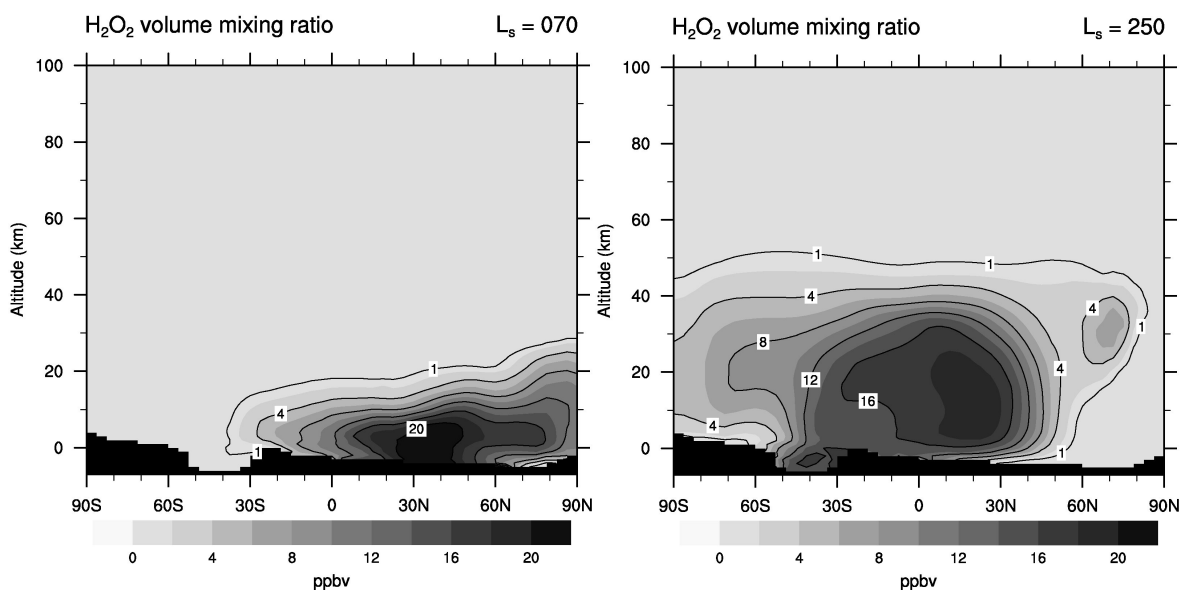


Figure 13.6. Zonally-averaged distribution of hydrogen peroxide H_2O_2 (ppbv) calculated by the LMD global climate model for daytime conditions at aphelion ($L_s = 70^\circ$, left) and perihelion ($L_s = 250^\circ$, right). The distribution of H_2O_2 is tightly correlated to that of its source HO_2 . From the model of Lefèvre *et al.* (2004).

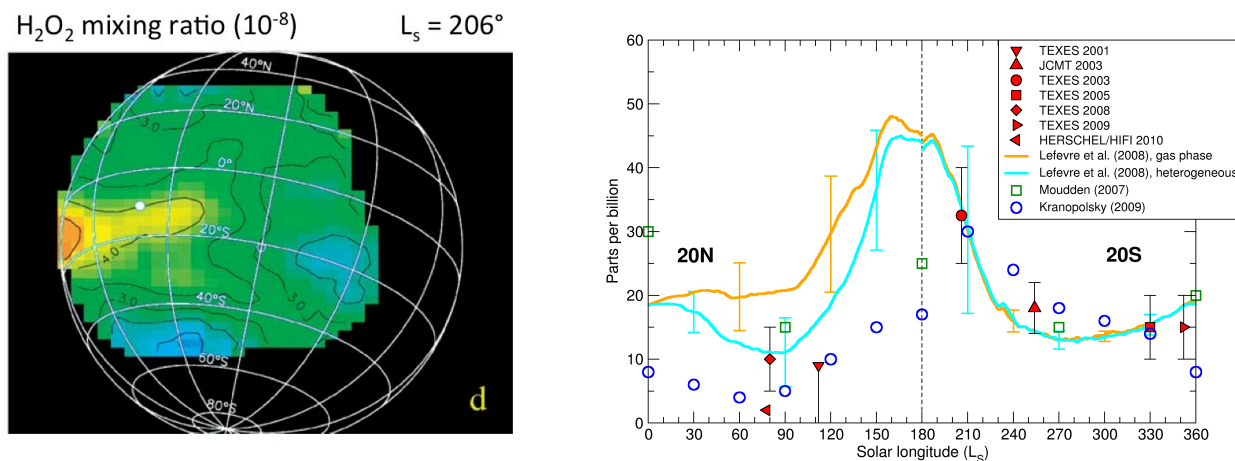


Figure 13.7. Observations of H_2O_2 on Mars. Left: First mapping of the H_2O_2 mixing ratio (units of 10^{-8}) obtained in June 2003 at $L_s = 206^\circ$ (Encrenaz *et al.*, 2004). Spatial variations are thought to be related to variations in H_2O amount. Right: the seasonal cycle of H_2O_2 on Mars. Observations in the infrared (TEXES) and models refer to 20°N for $L_s = 0-180^\circ$ and to 20°S for $L_s = 180-360^\circ$, in order to match as best as possible the observing conditions induced by the axial tilt of the planet. Submillimeter observations by Clancy *et al.* (2004, JCMT) refer to the entire disk. The points determined from Herschel at $L_s = 77^\circ$ (HERSCHEL/HIFI 2010) and TEXES 2001 at $L_s = 112^\circ$ are upper limits. GCM simulations updated from Lefèvre *et al.* (2008) ignore (yellow curve) or include (blue curve) heterogeneous chemistry. Error bars for the GCM represent variability (2σ). Model values by Krasnopolsky (2009) and Moudden (2007) are indicated by blue and green circles, respectively. Updated from Encrenaz *et al.* (2012).

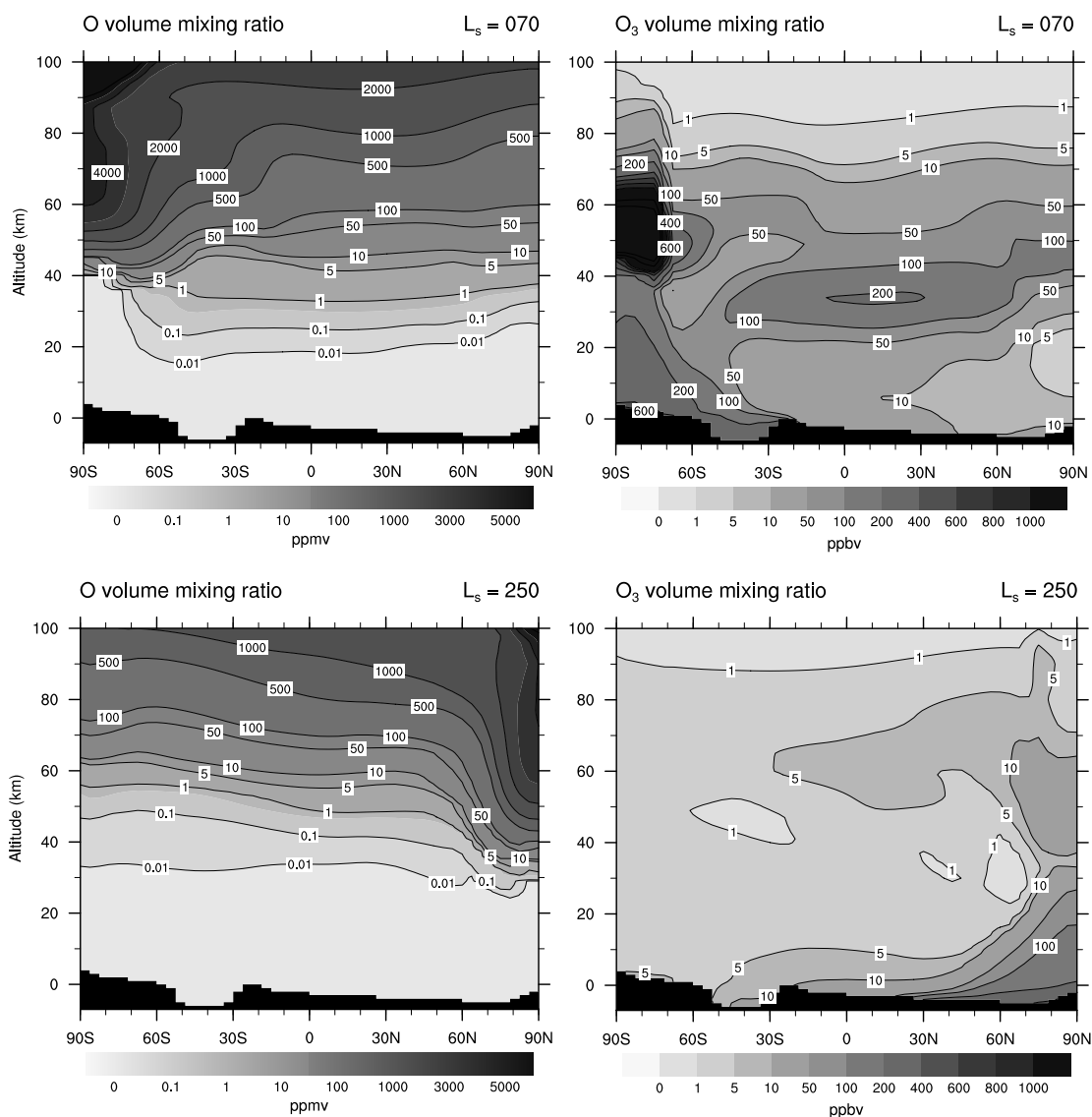


Figure 13.8. Zonally-averaged distribution of atomic oxygen O (left column, in ppmv) and ozone O₃ (right column, in ppbv) calculated by the LMD global climate model for daytime conditions. Top: near aphelion ($L_s = 70^\circ$). Bottom: near perihelion ($L_s = 250^\circ$). From the model of Lefèvre *et al.* (2004) after two martian years of simulation. Long-lived species O₂, CO, H₂ are chemically integrated but were initialized to their observed mean value (1.4×10^{-3} , 800 ppmv, 15 ppmv, respectively) at the beginning of the model run.

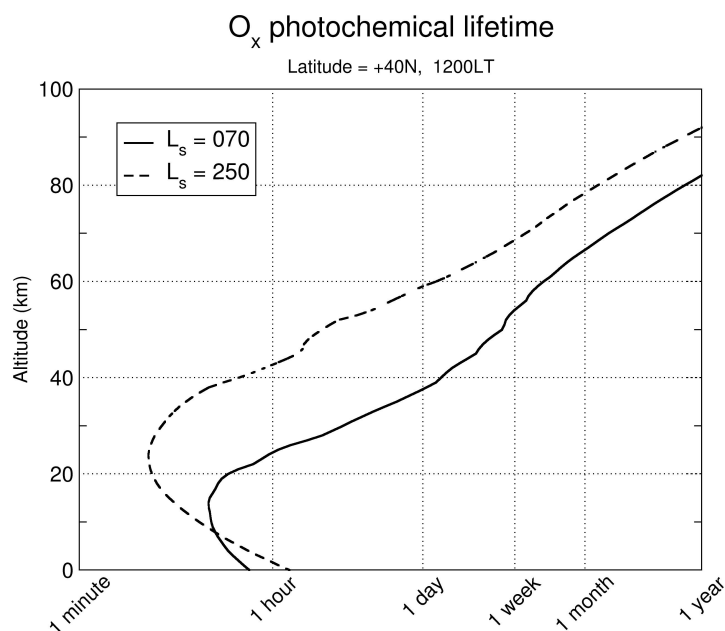


Figure 13.9. Mean photochemical lifetime of the O_x family (O + O(¹D) + O₃) calculated by the model of Lefèvre *et al.* (2004) at 40°N and local noon for L_s = 70° (solid curve) and L_s = 250° (dashed curve). Rise of the hygropause and the increase in upper atmosphere H₂O from aphelion to perihelion cause a dramatic reduction of the O_x lifetime above 20 km.

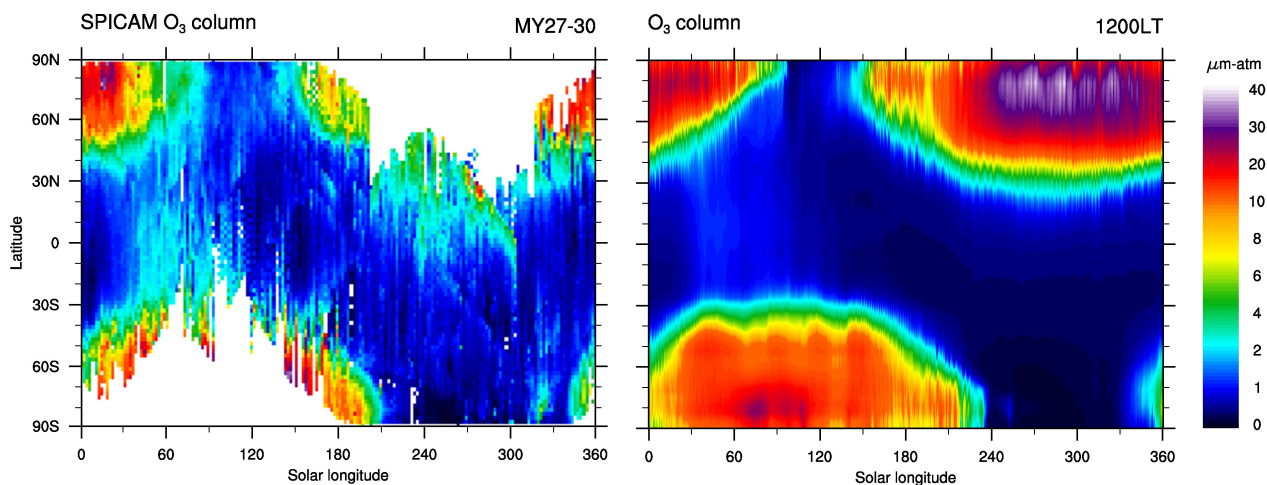


Figure 13.10. Seasonal evolution of the daytime ozone column ($\mu\text{m-atm}$). Left: ultraviolet measurements from the SPICAM instrument on Mars-Express averaged over martian years 27-30 (updated from Perrier *et al.*, 2006). Right: Three-dimensional simulation by the LMD global climate model with photochemistry described by Lefèvre *et al.* (2004), with updated kinetics and improved water cycle.

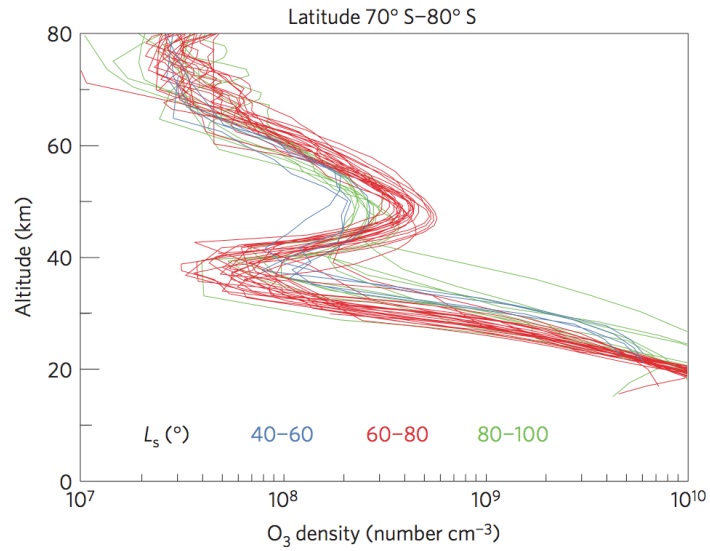


Figure 13.11. Nighttime O₃ vertical profile (molecule cm⁻³) observed from 2004 to 2011 by the SPICAM instrument on Mars-Express between 70°S and 80°S and covering L_s = 40°-100°. In the southern hemisphere polar night, a secondary maximum peaking at 50 km is detected above the near-surface O₃ layer that is typical of polar regions in winter. Dust opacity prevents the observation below ~20 km. From Montmessin and Lefèvre (2013).

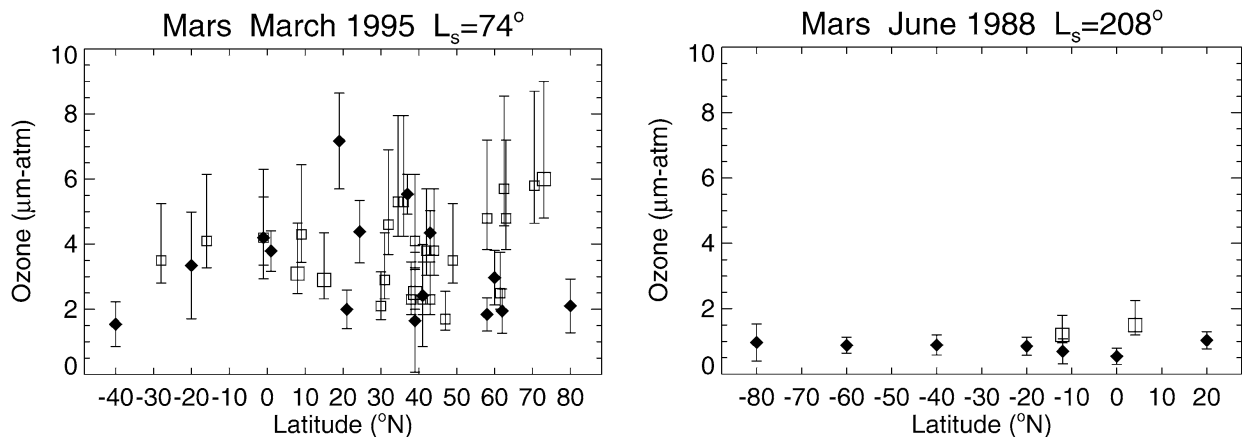


Figure 13.12. Ozone column ($\mu\text{m-atm}$) measured from Earth by infrared heterodyne spectroscopy (black symbols, Fast *et al.*, 2006; 2009) and from the Hubble Space Telescope Faint Object Spectrograph in the ultraviolet (open symbols, Clancy *et al.*, 1999). Left: Mars 1995, $L_s = 74^\circ$. Right: June 1988, $L_s = 208^\circ$.

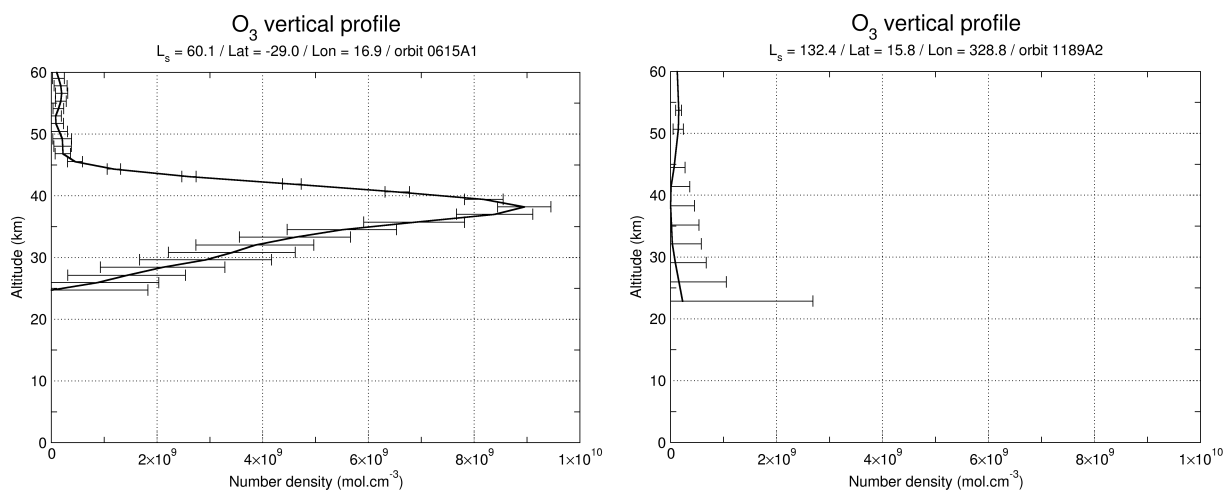


Figure 13.13. Examples of O₃ nighttime vertical profiles (molecules cm⁻³) measured at low latitudes. The data were obtained by stellar occultation with the SPICAM instrument on board Mars-Express. Left: near aphelion at $L_s = 60^\circ$ (29°S, 17°E). Right: in northern summer at $L_s = 132^\circ$ (16°N, 328°E). In both cases dust opacity prevents the observation below ~25 km. From Lebonnois *et al.* (2006).

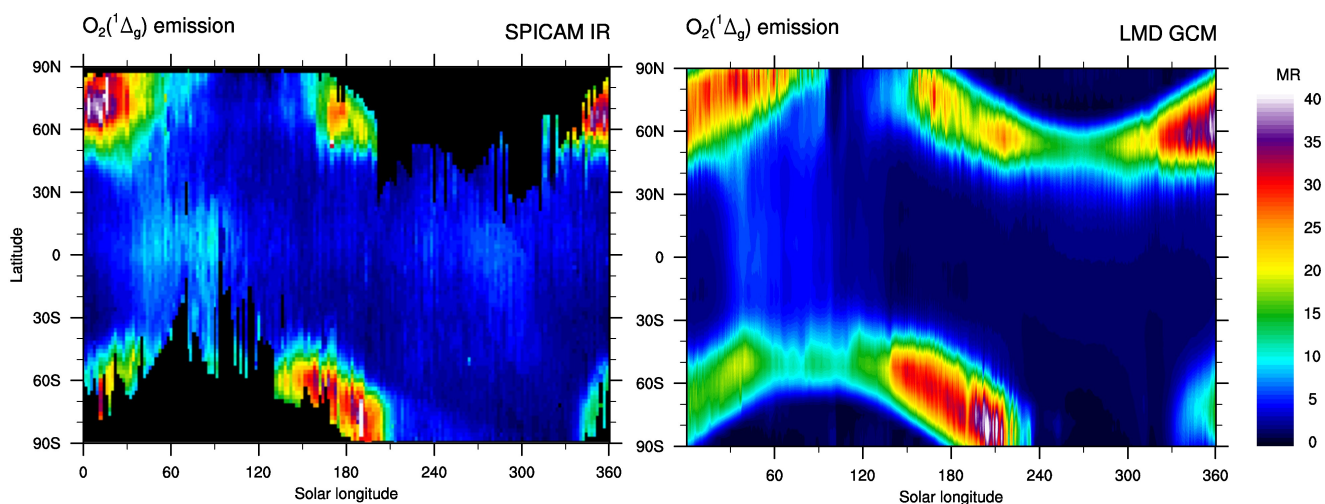


Figure 13.14. Seasonal evolution of the vertically-integrated $\text{O}_2(^1\Delta_g)$ dayglow at $1.27 \mu\text{m}$, in units of Mega-Rayleigh ($1 \text{ MR} = 10^{12} \text{ photons cm}^{-2} \text{ s}^{-1} (4\pi \text{ ster})^{-1} = 4.5 \times 10^{15} \text{ cm}^{-2} = 1.7 \mu\text{m-atm}$ for the dayglow at $1.27 \mu\text{m}$). Left: Satellite observations averaged over 2004-2012 with the infrared channel of SPICAM on Mars Express (updated from Fedorova *et al.*, 2006a). Right: Three-dimensional simulation by the LMD global climate model with photochemistry described by Lefèvre *et al.* (2004), with updated kinetics and improved water cycle. Calculations were made with a $\text{O}_2(^1\Delta_g)$ quenching rate by CO_2 equal to $0.5 \times 10^{-20} \text{ cm}^3 \text{ s}^{-1}$.

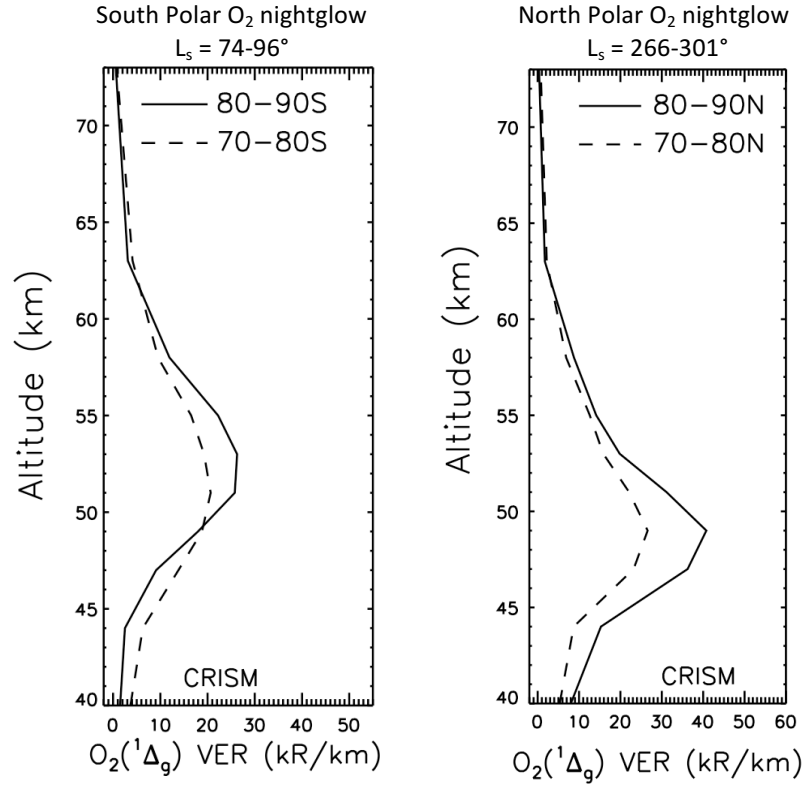


Figure 13.15. The $\text{O}_2(^1\Delta_g)$ nightglow observed over both polar regions by CRISM on Mars Reconnaissance Orbiter. Left: Averaged $\text{O}_2(^1\Delta_g)$ volume emission profiles (kR km^{-1}) over $L_s = 74^\circ\text{--}96^\circ$ for latitude bins of $70^\circ\text{S--}80^\circ\text{S}$ (dashed lines) and $80^\circ\text{S--}90^\circ\text{S}$ (solid lines). Right: Averaged $\text{O}_2(^1\Delta_g)$ volume emission profiles (kR km^{-1}) over $L_s = 266^\circ\text{--}301^\circ$ for latitude bins of $70^\circ\text{N--}80^\circ\text{N}$ (dashed lines) and $80^\circ\text{N--}90^\circ\text{N}$ (solid lines). From Clancy *et al.* (2012, 2013b).

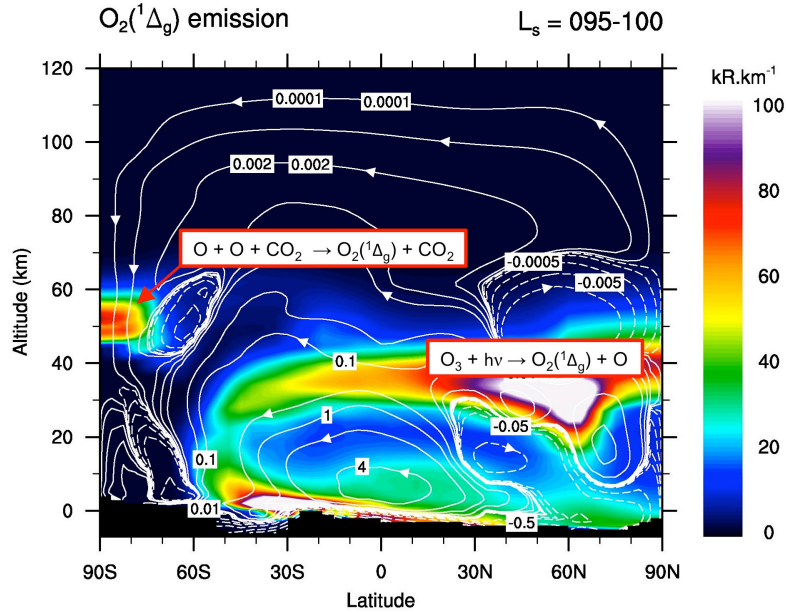


Figure 13.16. A schematic of the vertical and latitudinal distribution of the $O_2(^1\Delta_g)$ emission (zonally-averaged, in $kR km^{-1}$) as simulated by the LMD general circulation model for $L_s = 95^\circ$ - 100° . Two primary pathways exist for the production of $O_2(^1\Delta_g)$: 1) Over solar illuminated latitudes, the photolysis of ozone leads at this season to $O_2(^1\Delta_g)$ emission in a layer located above the hygropause between 25-40 km. A strong $O_2(^1\Delta_g)$ emission also outweighs the quenching by CO_2 near the surface in the southern hemisphere. This results from the dry surface conditions (see Figure 13.1) and subsequent large ozone densities at this season. 2) In the polar night, the three-body association of atomic oxygen transported downwards over the winter pole leads to $O_2(^1\Delta_g)$ emission between 45-60 km. The meridional stream function ($10^9 kg s^{-1}$) is superimposed in white contour lines. They visualize the downwelling branch of the winter hemisphere Hadley circulation, bringing large amounts of O atoms produced in the upper atmosphere towards lower altitudes into the polar night. From Clancy *et al.* (2012).

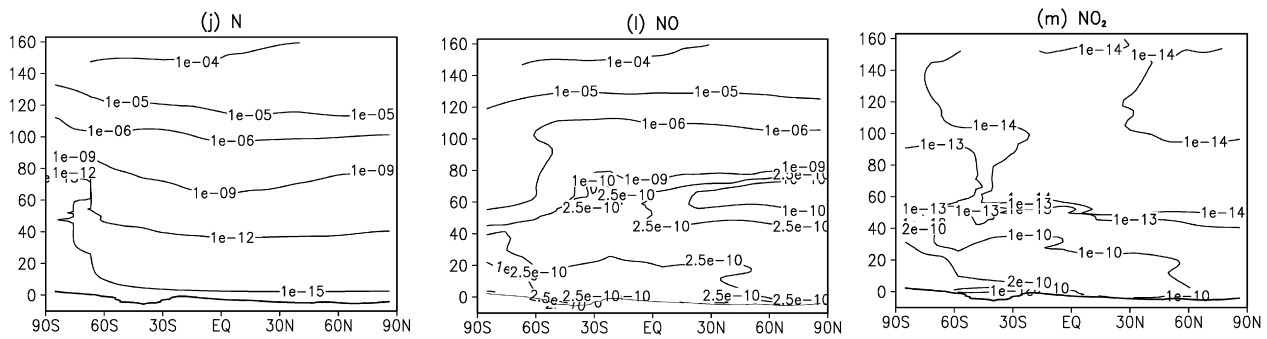


Figure 13.17. Latitude-altitude distribution of the mixing ratio (zonal mean) of the main nitrogen species N, NO, and NO₂ at $L_s = 90^\circ$, calculated by the general circulation model of Moudden and McConnell (2007).

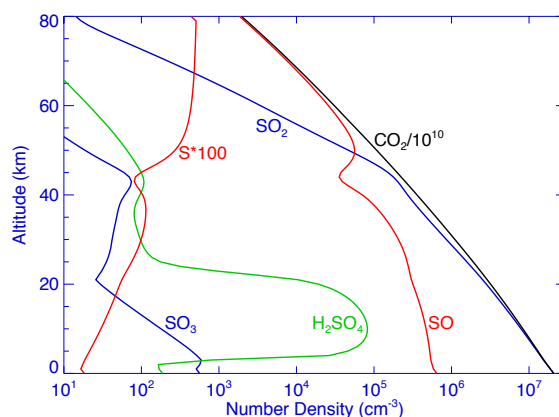


Figure 13.18. Vertical distribution of sulfur species (molecule cm^{-3}) for mean conditions below 80 km, assuming $\text{SO}_2 = 0.1$ ppbv at the surface. These results are obtained by inclusion of the SO_x chemistry in the 1D model of Krasnopolsky (2010). This chemistry involves updated data on photolysis of SO_2 and H_2SO_4 , reaction between SO_3 and H_2O , and heterogeneous reaction between SO_2 and H_2O_2 on ice particles. Uptake of H_2SO_4 on water-ice aerosols also occurs between 20-45 km and at night below 3 km. This explains the broad gas-phase H_2SO_4 peak between 3-20 km where uptake does not occur.

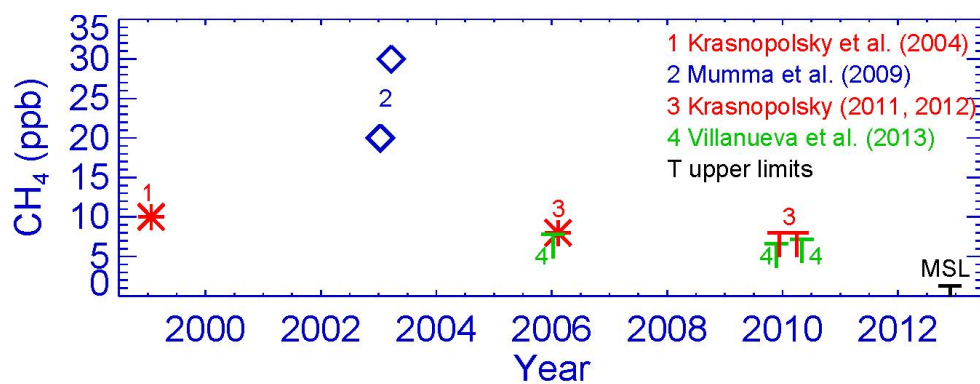


Figure 13.19. Mean methane mixing ratio (ppbv) derived from Earth-based (1999-2010) and MSL (2013) observations. “T” indicates upper limits. No methane has been detected after 2006.

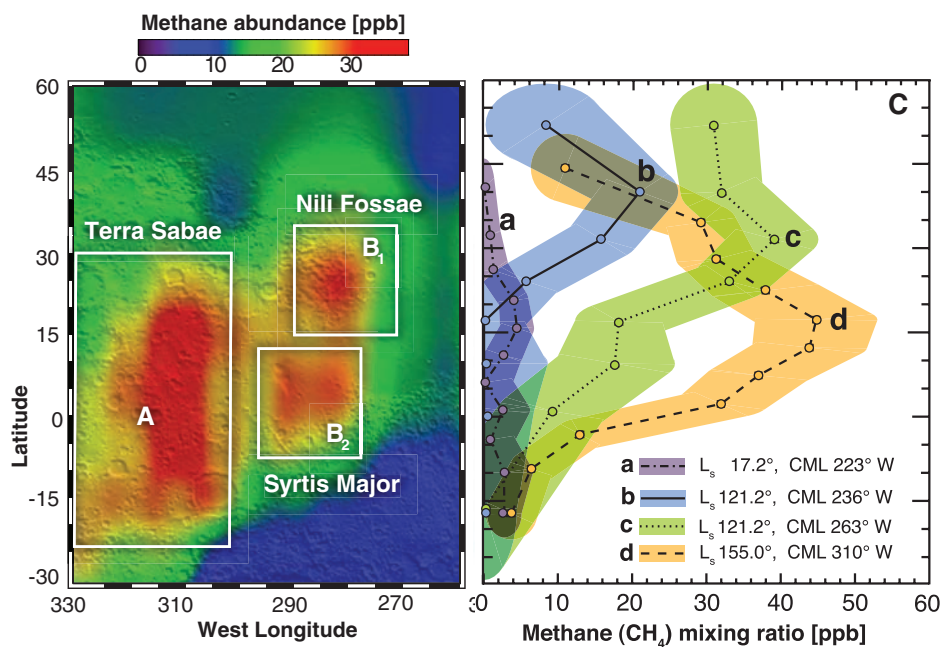


Figure 13.20. Methane mixing ratio (ppbv) observed from Earth by Mumma *et al.* (2009). Left: regions where methane appeared enhanced during summer 2003 ($L_s = 121^\circ$ - 155°). Right: latitudinal and temporal variability of methane. Profile a was obtained in February 2006 at $L_s = 17.2^\circ$. Profiles b, c, d were obtained in January-March 2003 between $L_s = 121^\circ$ - 155° .

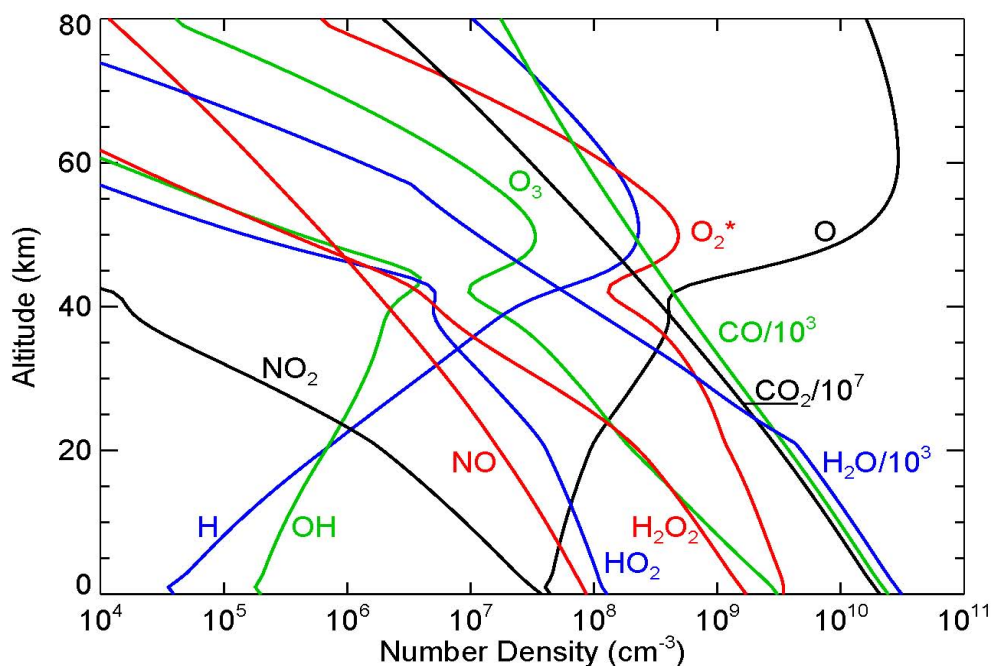


Figure 13.21. Density profiles (molecule cm^{-3}) calculated by the global-mean photochemical model of Krasnopolsky (2010), using the chemical reaction rates listed in Table 2. O_2^* is $\text{O}_2(^1\Delta_g)$. The surface pressure is set to 6.1 hPa and the H_2O vertical column is 9.5 precipitable microns. The H_2O density profile is restricted by the saturation value. A downward flow of O and CO from the dissociation of O_2 and CO_2 above 80 km is also imposed at the upper boundary. The calculated abundances of the major photochemical products are 1600 ppmv for O_2 , 120 ppmv for CO, 20 ppmv for H_2 , 0.9 $\mu\text{m-atm}$ for O_3 , 1.5 MR or 2.5 $\mu\text{m-atm}$ for $\text{O}_2(^1\Delta_g)$, and 7.6 ppbv for H_2O_2 . These values are in reasonable agreement with the observations, with the exception of CO that is underestimated by a factor of eight.

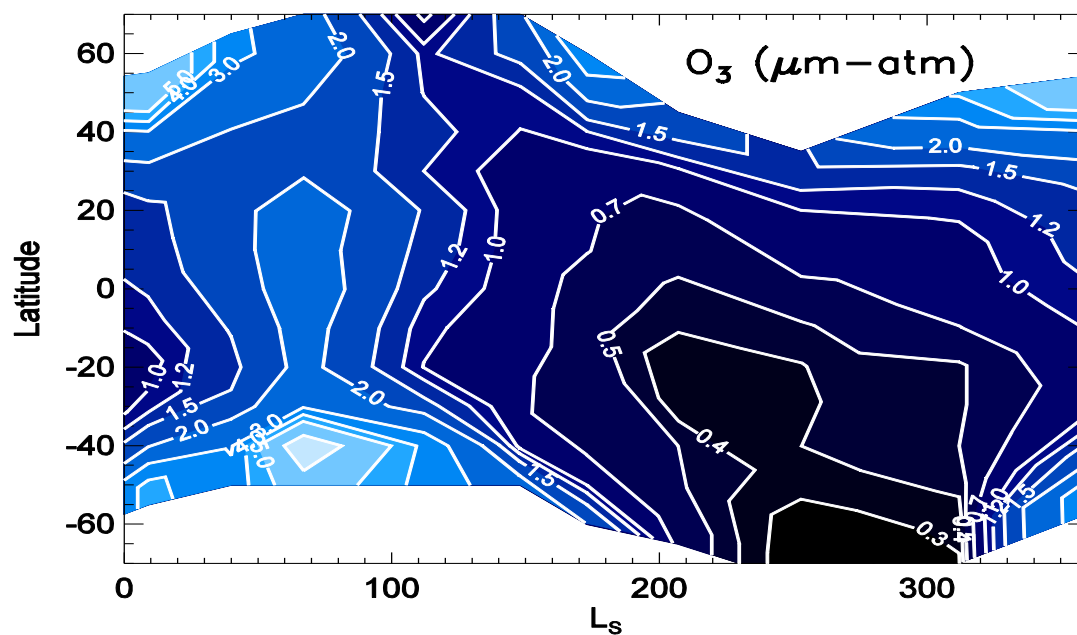


Figure 13.22. Ozone column ($\mu\text{m-atm}$) calculated by the 1D model of Krasnopolsky (2009) at different latitudes and seasons. The model includes an irreversible uptake coefficient of 3×10^{-4} for H_2O_2 on ice. This map can be compared to the SPICAM and ground-based observations of ozone displayed in Figures 13.10 and 13.12, respectively.

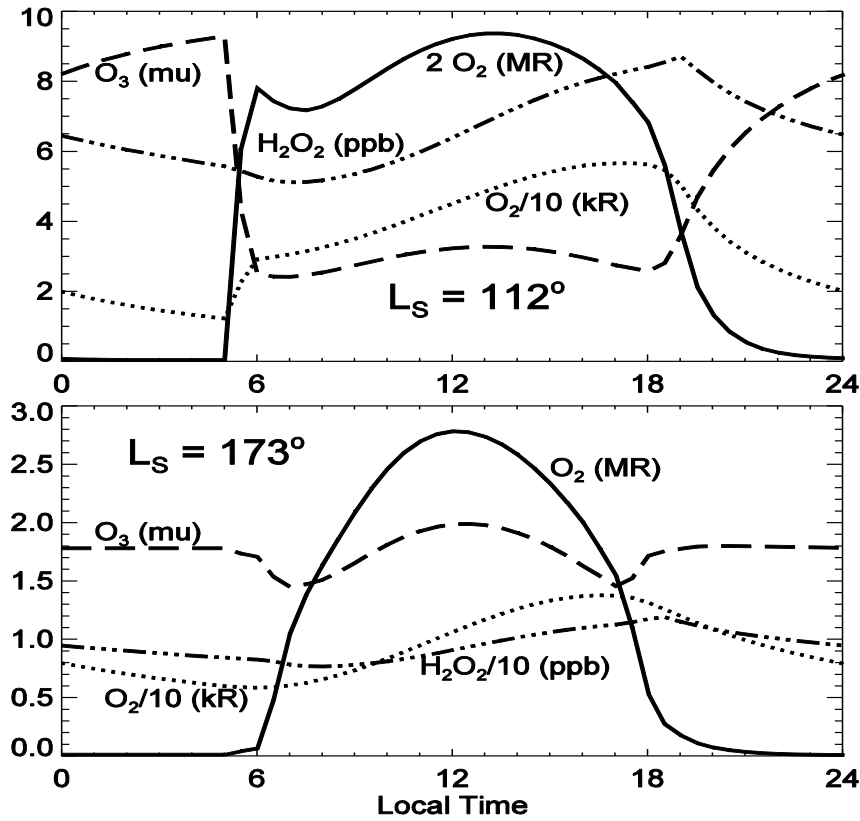


Figure 13.23. Modeled diurnal variations of the O₃ column (μm-atm), H₂O₂ (ppbv), the O₂(¹Δ_g) dayglow at 1.27 μm (solid line, in MR), and the O₂(¹Δ_g) airglow at 1.27 μm from the termolecular association of O atoms (dotted line, in kR). Top: results at L_s = 112°. Bottom: results at L_s = 173°. From Krasnopolsky (2006a).

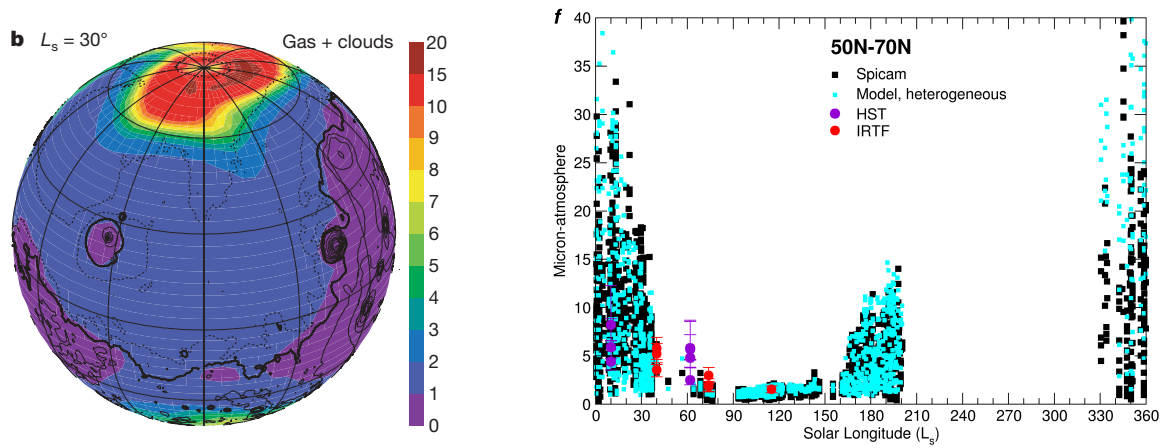


Figure 13.24. Ozone column ($\mu\text{m-atm}$) calculated by the LMD general circulation model. Left: synoptic distribution in northern spring ($L_s = 30^\circ$) with a photochemical scheme taking into account heterogeneous reactions of HO_x on water-ice clouds. The observer is facing the 180° meridian at local noon, and the black contours correspond to Mars topography. Right: Comparison of the same GCM simulation with the ozone columns measured in the 50°N - 70°N latitude band by SPICAM (Perrier *et al.*, 2006), HST (Clancy *et al.*, 1999), and IRTF (Fast *et al.*, 2006). From Lefèvre *et al.* (2008).

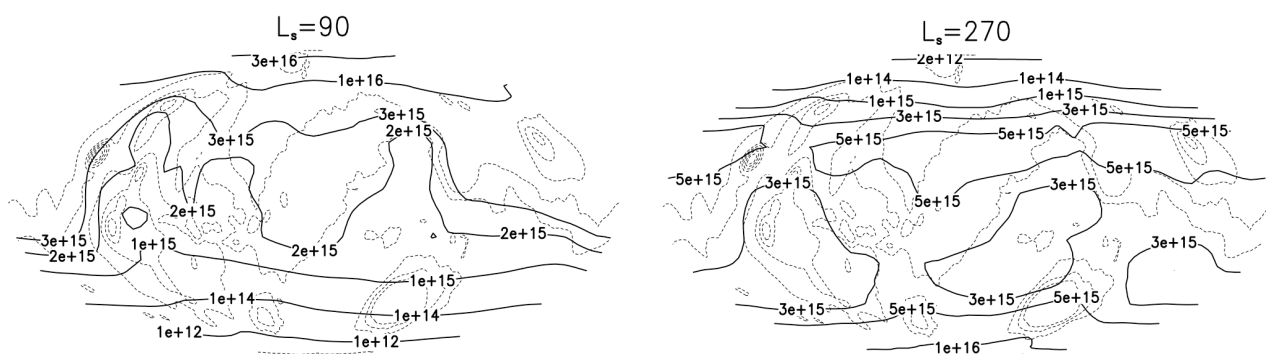


Figure 13.25. Column-averaged mixing ratio of H_2O_2 calculated by the GM3 general circulation model (Moudden and McConnell, 2007 ; Moudden, 2007). Left : $L_s = 90^\circ$. Right : $L_s = 270^\circ$. The seasonal evolution of H_2O_2 calculated by this model is compared to observations in the right panel of Figure 13.7.